

Untangling the chemical evolution of Titan's atmosphere and surface—from homogeneous to heterogeneous chemistry

Ralf I. Kaiser,^{*a} Pavlo Maksyutenko,^a Courtney Ennis,^a
Fangtong Zhang,^a Xibin Gu,^a Sergey P. Krishtal,^b
Alexander M. Mebel,^{*b} Oleg Kostko^c and Musahid Ahmed^{*c}

Received 24th February 2010, Accepted 7th April 2010

DOI: 10.1039/c003599h

In this article, we first explored the chemical dynamics of simple diatomic radicals (dicarbon, methylidyne) utilizing the crossed molecular beams method. This versatile experimental technique can be applied to study reactions relevant to the atmospheres of planets and their moons as long as intense and stable supersonic beam sources of the reactant species exist. By focusing on reactions of dicarbon with hydrogen cyanide, we untangled the contribution of dicarbon in its singlet ground and first excited triplet states. These results were applied to understand and re-analyze the data of crossed beam reactions of the isoelectronic dicarbon plus acetylene reaction. Further, we investigated the interaction of ionizing radiation in form of energetic electrons with organic molecules ethane and propane sequestered on Titan's surface. These experiments presented compelling evidence that even at irradiation exposures equivalent to about 44 years on Titan's surface, aliphatic like organic residues can be produced on Titan's surface with thicknesses up to 1.5 m. Finally, we investigated how Titan's nascent chemical inventory can be altered by an *external* influx of matter as supplied by (micro)meteorites and possibly comets. For this, we simulated the ablation process in Titan's atmosphere, which can lead to ground and electronically excited atoms of, for instance, the principal constituents of silicates like iron, silicon, and magnesium, in laboratory experiments. By ablating silicon species and seeding the ablated species in acetylene carrier gas, which also acts as a reactant, we produced organo silicon species, which were then photoionized utilizing tunable VUV radiation from the Advanced Light Source. In combination with electronic structure calculations, the structures and ionization energies of distinct organo-silicon species were elucidated.

1. Introduction

The arrival of the Cassini–Huygens probe at Saturn's moon Titan – the only Solar System body besides Earth and Venus with a solid surface and a thick atmosphere with a pressure of 1.4 atm at surface level – in 2004 opened up a new chapter in the history of Solar System exploration. The mission revealed Titan as a world with striking Earth-like landscapes involving hydrocarbon lakes¹ and seas as well as sand dunes² and lava-like features³ interspersed with craters and icy mountains of

^aDepartment of Chemistry, University of Hawaii at Manoa, Honolulu, HI, 96822, USA

^bDepartment of Chemistry & Biochemistry, Florida International University, Miami, 33199, USA

^cChemical Sciences Division, Lawrence Berkeley National Laboratory, Berkeley, California, 94720, USA

hitherto unknown chemical composition.⁴ The discovery of a dynamic atmosphere and active weather system⁵ illustrates further the similarities between Titan and Earth.⁶ The aero-based haze layers,⁷ which give Titan its orange-brownish color, are not only Titan's most prominent optically visible features,⁸ but also play a crucial role in determining Titan's thermal structure and chemistry.⁹ These smog-like haze layers are thought to be very similar to those that were present in Earth's atmosphere before life developed more than 3.8 billion years ago, absorbing the destructive ultraviolet radiation from the Sun, thus acting as 'prebiotic ozone' to preserve astrobiologically important molecules on Titan. Compared to Earth, Titan's low surface temperature of 94 K and the absence of liquid water preclude the evolution of biological chemistry as we know it. Exactly because of these low temperatures, Titan provides us with a unique prebiotic "atmospheric laboratory" yielding vital clues – at the frozen stage – on the likely chemical composition of the atmosphere of the primitive Earth. However, the underlying chemical processes, which initiate the haze formation from simple molecules, have been not understood well to date.

Titan's chemical inventory is the result of a rich, coupled photochemistry of two main atmospheric constituents: molecular nitrogen (N_2) and methane (CH_4).¹⁰ Stratospheric trace constituents have been firmly identified *via* infrared spectroscopy on board the Voyager I and II spacecrafts¹¹ as well as in the framework of the Cassini–Huygens mission.¹² These are the hydrocarbon molecules acetylene (C_2H_2), ethylene (C_2H_4), ethane (C_2H_6), methylacetylene (CH_3CCH), propane (C_3H_8), diacetylene (C_4H_2), and benzene (C_6H_6), several nitriles like hydrogen cyanide (HCN), cyanoacetylene (HCCCN), cyanogen (C_2N_2), and dicyanodiacetylene (C_6N_2), as well as oxygen-bearing molecules carbon dioxide (CO_2), carbon monoxide (CO), and water (H_2O). The emission lines of these molecules can be utilized as valuable tracers to collect data on temperature profiles, on the potential existence of cold

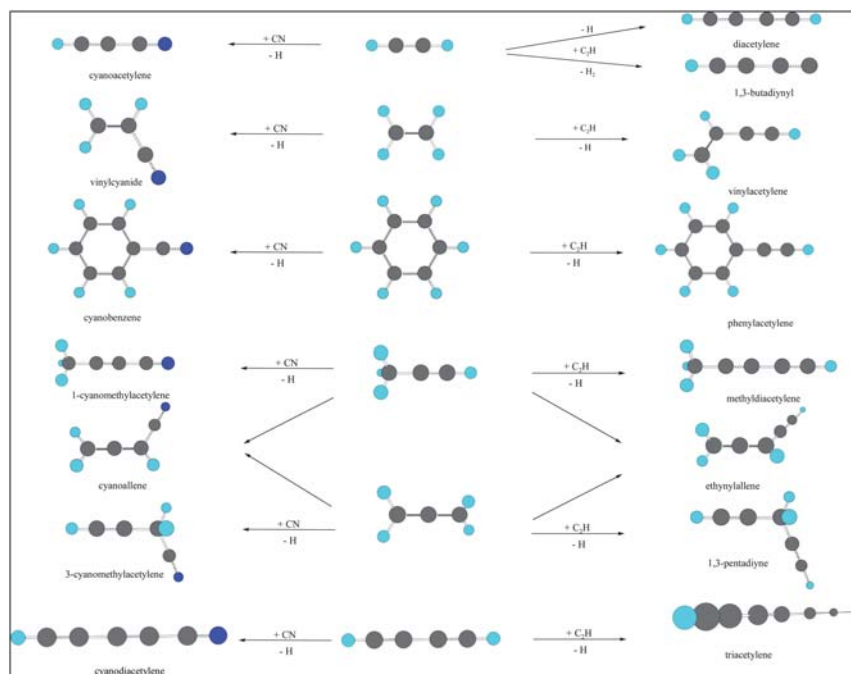


Fig. 1 Products formed in the bimolecular reactions of cyano ($CN(X^2\Sigma^+)$) and ethynyl radicals ($C_2H(X^2\Sigma^+)$) with unsaturated hydrocarbons.¹⁰⁹

traps and freeze-out zones, and on molecular abundances in the stratosphere; they also help to understand the formation of the organic aerosol layers on Titan. Here, planetary chemists proposed that the formation of the aerosol layers is initiated by fast and barrierless reactions of small, carbon-bearing radicals such as simple diatomics (dicarbon, $C_2(X^1\Sigma_g^+/a^3\Pi_u)$;^{13,14} methylidyne radicals, $CH(X^2\Pi_g)$;¹⁵ cyano radicals, $CN(X^2\Sigma^+)$ ¹⁶) and triatomic molecules like the ethynyl radical ($C_2H(X^2\Sigma^+)$)^{17,18} with unsaturated hydrocarbons *via* organic transient species. These considerations have led to the development of photochemical models of Titan¹⁹ and also to extensive laboratory studies during the last decades.^{8,20} However, the majority of these experiments were performed under bulk conditions.²¹ Several limitations such as wall effects undermine their validity.²² Also, the reaction products are often analyzed off-line and *ex situ*.²³ Hence, the detailed chemical dynamics of the reaction – the role of radicals and intermediates – cannot always be obtained, and reaction mechanisms can at best be inferred indirectly and qualitatively. Recently, a different experimental approach has been utilized. By conducting a series of detailed experiments on the elementary steps of cyano and ethynyl radical reactions and photodissociation studies of hydrocarbon molecules, a complete picture of the processes involved in the chemical processing of Titan's atmosphere is beginning to emerge. Since the macroscopic alteration of Titan's atmosphere consists of multiple elementary reactions that are a series of bimolecular encounters between radicals and molecules, this detailed understanding of the mechanisms involved at the microscopic level is crucial to unravel the chemical evolution and processing of low temperature environments in general. These are experiments under single collision conditions in which particles of one supersonic beam are made to 'collide' only with particles of a second beam (reactive collisions) or photons (photodissociation). Here, crossed beam experiments of cyano ($CN(X^2\Sigma^+)$)²⁴ and ethynyl radicals ($C_2H(X^2\Sigma^+)$)¹⁷ with unsaturated hydrocarbons demonstrated that highly unsaturated nitriles – organic molecules carrying the cyano (CN) group – and hydrogen-deficient molecules, among them (substituted) polyynes up to triacetylene, can be formed (Fig. 1). Low temperature kinetic experiments of cyano and ethynyl radicals amplified the role of these neutral-neutral reactions in Titan's low temperature atmosphere as these studies depicted the barrierless nature of bimolecular encounters of ethynyl and cyano radicals with rate constants of a few $10^{-10} \text{ cm}^3 \text{ s}^{-1}$ being close to the gas kinetics limit.^{14,25}

Among the diatomic species, closed shell, ground state dicarbon $C_2(X^1\Sigma_g^+)$ and its open shell first excited triplet state $C_2(a^3\Pi_u)$ counterpart have received considerable attention. In Titan's atmosphere, dicarbon can be formed as a transient species *via* photodissociation of the ethynyl radical, $C_2H(X^2\Sigma^+)$; the latter is the primary photodissociation product of acetylene (C_2H_2) at a wavelength less than 217 nm (5.7 eV).^{26,27} Reactions of singlet and triplet dicarbon with unsaturated hydrocarbons such as acetylene and ethylene were shown to be rapid over the temperature range of 24 K to 300 K with reaction rates larger than $10^{-10} \text{ cm}^3 \text{ s}^{-1}$ for singlet dicarbon; reactions of triplet dicarbon were systematically slower than their singlet counterparts.^{13,28} Nevertheless, since only the decay kinetics of the dicarbon reactants were followed, information on the reaction products were elusive. A series of crossed molecular beam experiments, in which reaction products can be identified under single collision conditions, unraveled a rich chemistry (Fig. 2) leading not only to hydrogen-terminated, polyyne-like carbon clusters (C_nH ($n = 4, 6$)), but also to resonantly stabilized free radicals (RSFR) of the generic formula C_nH_3 ($n = 4, 5$) – potential building blocks to form aromatic molecules in Titan's atmosphere. Since the electronic ground and first excited triplet states are very close in energy (718 cm^{-1}), they are both present in the crossed molecular beam studies and – due to the absence of any entrance barrier – both react with the hydrocarbon reactant. However, a recent crossed beam study of the reaction of dicarbon with hydrogen cyanide (HCN) provided evidence that at low collision energies, only singlet dicarbon reacted.²⁹ This system presents an unprecedented opportunity to discriminate

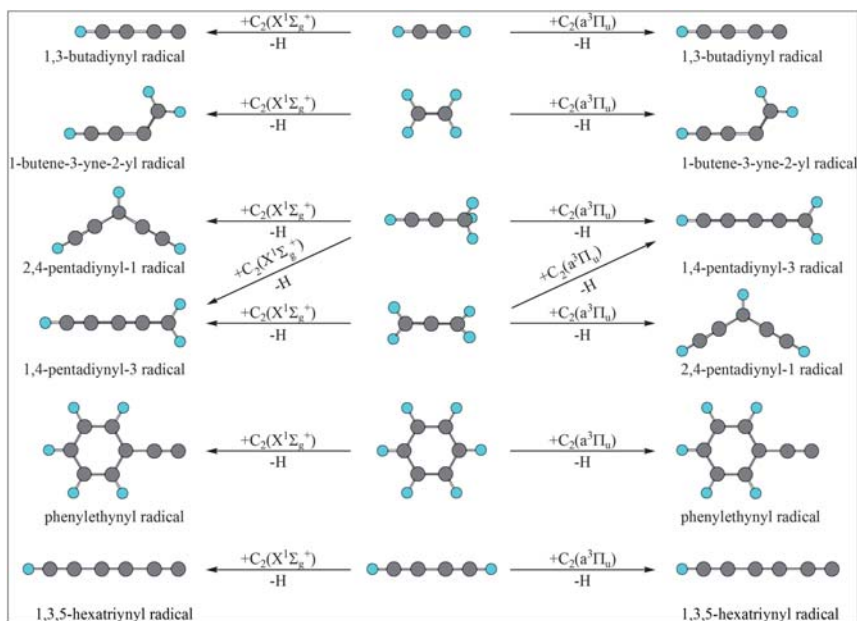
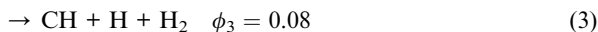
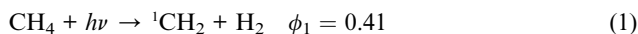


Fig. 2 Products formed in the bimolecular reactions of ground and excited states dicarbon $C_2(X^1\Sigma_g^+/a^3\Pi_u)$ with unsaturated hydrocarbons.¹⁰⁹

the reaction dynamics of ground state (lower collision energy) and triplet dicarbon molecules, which reacts only at higher collision energies due to a barrier in the entrance channel of at least 29.3 kJ mol^{-1} . Therefore, we conducted the reaction of dicarbon molecules in both their singlet and triplet states with hydrogen cyanide at a collision energy of 42.4 kJ mol^{-1} and compare the findings with our previous study on the singlet surface. Note that our experimental collision energies are higher than the equivalent temperature conditions in Titan's atmosphere. Does this have any effect on the implications of these studies to Titan's chemistry? For this purpose, we have combined our experiments with electronic structure calculations (see below); the combined experimental and theoretical data suggest that only one reaction channel is open – at all temperatures and collision energies above the threshold. However, in case of multiple reaction pathways and product isomers, it is important to account for the collision-energy (and temperature) dependent change in the branching ratios of distinct product isomers formed. These findings are then applied to untangle the chemical dynamics of the isoelectronic dicarbon–acetylene system on the singlet and triplet surface. Recall that previous studies of this reaction not only failed to discriminate between the chemical dynamics on the singlet and triplet surface, but also led to contradictory results when comparing studies with continuous³⁰ and pulsed dicarbon beams.³¹

We also present preliminary data on the reactions of important methylidyne radicals ($CH(X^2\Pi_u)$). Recall that in Titan's atmosphere, the methylidyne radical is expected to play a role in synthesizing higher hydrocarbon molecules. Since methane (CH_4) presents the most abundant hydrocarbon on Titan, the photolysis of methane is considered as the major source of methylidyne. Lacking an unsaturated bond, methane only absorbs light shorter than 145 nm ; therefore, the photochemistry of methane mostly occurs in the stratosphere with a significant flux of Lyman- α photons at 121.6 nm (10.2 eV). Early laboratory works by McNesby *et al.*,³² Laufer *et al.*,³³ Gorden *et al.*,³⁴ Rebert *et al.*,³⁵ and Slinger *et al.*³⁶ suggested quantum yields (denoted ϕ) for methane photolysis at 121.6 nm as defined by eqn (1)–(4). Secondary processes were inferred to produce the methylidyne radical *via* reactions

(5)–(7).³⁷ In a recent theoretical study, Lodrighito *et al.*³⁸ investigated the photodissociation processes of methane theoretically on its lowest singlet potential surface at 122 nm. They found that non-adiabatic dynamics were important, and methyl ($\text{CH}_3(\text{X}^2\text{A}''_2)$) plus atomic hydrogen and the carbene ($\text{CH}_2(\text{a}^1\text{A}_1)$) plus molecular hydrogen were the major dissociation channels. The methyl radical was mostly formed *via* direct dissociation hopping to the ground state. On the other hand, carbene can either be formed by hopping to the ground state surface or through adiabatic dissociation involving carbene in its b^1B_1 state. They also suggested that the triple dissociation channel $\text{CH} + \text{H}_2 + \text{H}$ was less important; methylidyne is formed *via* a two step sequential mechanism, where either a molecular or atomic hydrogen elimination was followed by a atomic or molecular hydrogen loss. Later, Zhang *et al.*³⁹ reinvestigated this reaction utilizing the high resolution Rydberg tagging time-of-flight (TOF) technique after photo dissociating methane at 130 nm. Their results show an important single C–H bond fission channel from methane. A simulation of the TOF spectra indicated the formation of highly rotationally excited methyl radicals. These products are attributed to the conical intersection pathway between the excited state singlet (S_1) and ground state singlet (S_0) surface of methane.



However, due to the difficulty to probe quantitatively the hydrocarbon fragments, the branching ratios are debatable. Lee *et al.*,⁴⁰ for instance, reported excitation spectra of electronically excited carbene $\text{CH}_2(\text{a}^1\text{B}_1)$ showing that this channel is only a minor pathway in the methane photolysis. Utilizing the technique of hydrogen atom photofragment translational spectroscopy, Mordaunt *et al.*⁴¹ found a simple carbon-hydrogen bond fission in methane to be the dominant primary process at 121.6 nm. The resulting methyl radical (CH_3) fragments are formed with sufficient internal energy that about 25% of them undergo secondary decomposition yielding predominantly methylidyne (CH) and molecular hydrogen (H_2). Brownsword *et al.*⁴² measured the absolute hydrogen atom quantum yield as 0.47 for the methane Lyman- α photolysis in agreement with the conclusions of Mordaunt *et al.* Later, Mebel *et al.*'s⁴³ *ab initio* calculation and experimental works by Heck

et al. and Wang *et al.* revealed that at 121.6 nm, the methyl radical channel can be considered as the major pathway.^{27,44} Consequently, the methylidyne branching ratio should be higher than 0.08 as proposed originally. Kinetic studies in the range of 23 K to 295 K indicate that subsequent reactions of the methylidyne radical with hydrocarbon molecules are fast (few 10^{-10} $\text{cm}^3 \text{s}^{-1}$) and in the case of olefins, hold maximum rate constants at around 70 K.¹⁵ Utilizing tunable vacuum ultraviolet (VUV) photoionization and time-resolved mass spectrometry, Leone and co-workers suggested that at 298 K, methylidyne reacts with ethylene to form $70 \pm 8\%$ allene (H_2CCCH_2), $30 \pm 8\%$ methylacetylene (CH_3CCH), and less than 10% cyclopropene ($\text{c-C}_3\text{H}_4$). Experiments with acetylene indicated the formation of mainly the cyclic C_3H_2 isomer with smaller fractions of triplet propargylene (HCCCH), in contrast to theoretical predictions. However, the authors emphasized that since the experiments were not conducted under single collision conditions, atomic hydrogen-triggered isomerization processes were likely responsible to change the nascent product distribution.⁴⁵ Therefore, experiments conducted under single collision conditions as provided in crossed molecular beams, in which the nascent reaction products can be probed, are clearly desired.

Secondly, since the gaseous molecules might also agglomerate to aerosol particles⁴⁶ or sequester to Titan's surface,⁴⁷ we also present new data on the interaction of potentially abundant organic solids (ethane, propane) with ionizing radiation in the form of energetic electrons, as generated in the track of high energy galactic cosmic ray particles. In a pioneering study, Sagan and Thomas outlined that energetic cosmic ray particles can penetrate deep into the lower atmospheric layers.⁴⁸ These energetic particles could incorporate part of their kinetic energy into chemical reaction and thus process simple organics in Titan's lower atmosphere. In a more recent study, Molina-Cubero *et al.* derived an energy deposition on Titan's surface of 4.5×10^9 $\text{eV cm}^{-2} \text{s}^{-1}$.⁴⁹ However, the radiation processing of these simple organics by energetic electrons is not well understood. To shed light on this matter and to gain a comprehensive picture of the hydrocarbon chemistry, not only in the gas phase as described above but also in the condensed phase, we present data on the interaction of ionizing radiation, in form of energetic electrons, with solid ices of ethane and propane – two of Titan's abundant saturated hydrocarbons. We will also investigate to what extent the radiation processing can lead to the formation of polymer-like macromolecules, which could present building blocks of Titan's organic aerosol layers, *via* heterogeneous chemistry.⁵⁰

Finally, it has to be noted that Titan's nascent chemical inventory can be not only enriched, but also altered by an *external* influx of matter as supplied by (micro)meteorites and possibly comets.^{51,52} Therefore, these processes must also be understood to gain a complete picture of the chemical inventory. Recent photochemical models suggest that Titan's oxygen-bearing species (carbon monoxide, carbon dioxide, and water) can be simultaneously reproduced using an oxygen flux consistent with the Cassini Plasma Spectrometer observations and a hydroxyl radical (OH) flux consistent with the predicted production from (micro)meteorite ablation.⁵² The impact of (micro)meteorites with dense atmospheres also leads to an ablation of the nascent meteoritic material thus releasing ground and excited metal atoms (mostly iron (Fe), magnesium (Mg), and silicon (Si) from abundant silicates) and their ions.⁵³ As discussed by Petrie,⁵⁴ within the hydrocarbon-rich atmosphere of Titan, these species are expected to form unsaturated and polar organo-metallic molecules, which could provide effective nucleation sites for the condensation of polar molecules and highly unsaturated hydrocarbon molecules at high altitudes. This in turn could lead to metal- and silicon-doped tholin-like material. Although extensive work has been conducted on magnesium-bearing molecules,⁵³ an understanding of the organo-silicon chemistry is still in its infancy; only a single crossed molecular beam study on the reactions of ground state silicon atoms with acetylene has been conducted to date.⁵⁵ There have been a few theoretical studies on the ionization energy of $\text{Si}(\text{C}_2\text{H}_2)$, and very early electron impact measurements for a few silicon

carbides with large error uncertainties of a few tenths of an electron volt, but beyond this there is a paucity of information regarding organo-silicon compounds.⁵⁶ Due to this lack of data on silicon-carbon-bearing molecules, we report here on the *in situ* reaction of ablated silicon species – as simulated by laser ablation of neat silicon – with acetylene acting as a prototype unsaturated hydrocarbon molecule in Titan's atmosphere. These studies provide not only an inventory of potentially abundant neutral organo-silicon molecules in Titan's atmosphere, but also deliver accurate ionization energies of these molecules. The ionization energies are in turn crucial to predict to what extent newly formed organo-silicon molecules can be ionized in Titan's atmosphere by the harsh UV/VUV radiation field from the Sun possibly influencing the charge balance in Titan's upper atmosphere.

At this *Faraday Discussion*, we cover three fields of interest related to Titan's chemical evolution. First, we present the crossed molecular beams approach which can be applied to study bimolecular reactions in Titan's atmosphere. Data on the reactions of excited state dicarbon molecules with hydrogen cyanide (HCN) and of methylidyne radicals with methylacetylene (CH₃CCH) and diacetylene (C₄H₂) are discussed. Hereafter, we move to solid state chemistry and describe to what extent the interaction of ionizing radiation with closed shell hydrocarbons, ethane (C₂H₆) and propane (C₃H₈), present either in aerosol droplets and/or sequestered on Titan's surface can lead to the formation of an organic 'polymer' and hence influence the overall hydrocarbon budget. Finally, we present novel data on the formation and ionization energies of silicon-bearing organic molecules, which are of possible interest to understand the reactions of (micro)meteoritic ablated silicon atoms with acetylene in Titan's upper atmosphere.

2. Experimental approach

2.1. The crossed molecular beams setup

2.1.1. The crossed molecular beams approach. Which experimental approach can be utilized to expose the chemical dynamics of reactions of diatomic molecules such as ground (C₂(X¹Σ_g⁺)) and excited state dicarbon (C₂(a³Π_u)) molecules as well as the methylidyne radical (CH(X²Π_g)) in Titan's hydrocarbon-rich atmosphere? Since the macroscopic alteration of atmospheres of planets and their moons involves multiple elementary reactions, that are a series of *bimolecular encounters*, a detailed understanding of the mechanisms involved at the most fundamental, microscopic level by eliminating any wall effects is desirable. These are experiments conducted under single collision conditions, in which particles of one supersonic beam – predominantly an unstable species such as dicarbon or methylidyne – are made to 'collide' only with particles of a second supersonic beam.^{57,58} In strong contrast to bulk experiments, where reactants are mixed and where the product distribution might be influenced by wall effects of the reactant vessel, the crossed beam approach has the unique capability of generating the radicals in separate supersonic beams. In principle, both reactant beams can be prepared in well-defined quantum states before they cross at a specified energy under single collision conditions. This provides an unprecedented opportunity to observe the consequences of a single collision event, excluding secondary collisions and most importantly wall effects. In principle, the products can be detected *via* spectroscopic detection schemes such as laser induced fluorescence (LIF)⁵⁹ or Rydberg tagging,⁶⁰ ion imaging probes,^{61,62} or *via* a quadrupole mass spectrometric detector (QMS) with universal electron impact ionization or photoionization. Crossed beam experiments can therefore help to untangle the chemical dynamics, to infer the intermediates, and to identify the nascent reaction products under single collision conditions; neither bulk nor kinetic experiments can supply this information. It should be mentioned that recent kinetics experiments pioneered an isomeric-specific detection of reaction products utilizing time-resolved multiplexed photoionization mass spectrometry *via* synchrotron radiation.⁶³ Under

those experimental conditions, the reaction intermediates may undergo up to a few thousand collisions with the bath molecules so that three-body encounters cannot be eliminated, and true single collision conditions are not provided. On the other hand, in 'real' atmospheres, stabilizations due to collisions are important if the collision times are shorter than the lifetime of the reaction intermediates, and they can be only probed in collisional environments. Therefore, crossed beams and kinetics studies must be regarded as highly complementary.

Over the past decades, the use of crossed molecular beams has led to an unprecedented advancement in our understanding of fundamental principles underlying chemical reactivity. Detailed experimental studies of simple three-atom reactions established experimental benchmarks such as the reactions of chlorine,⁶⁴ fluorine,⁶⁵ deuterium,⁶⁶ carbon,⁶⁷ nitrogen,⁶⁸ oxygen,⁶⁹ and sulfur atoms⁷⁰ with molecular hydrogen. This approach has been extended to tetra atomic systems like OH/CO⁷¹ and OH/H₂ together with their isotopic variants,⁷² and CN/H₂ (D₂).⁷³ These simple systems are prototypical reactions in bridging our theoretical understanding of reactive scattering, *via* dynamics calculations on chemically accurate potential energy surfaces, with experimental observations.⁷⁴ These dynamics calculations are needed to turn the *ab initio* results into quantities that can be compared with experiments. Quasi classical trajectory (QCT) calculations are of particular significance to investigate the effect of the collision energy on the chemical dynamics and to derive the experimental observables such as the collision energy dependence of the reaction cross section, the translational energy and angular distributions, and the differential cross section as a function of the center-of-mass angle and product center of mass velocity. Although interest in these light elementary reactions still continues, with the development of powerful theoretical models, attention has turned during the last years to more complex systems of significant practical interest such as in combustion processes,^{62,75} catalysis,⁷⁶ atmospheric chemistry,⁷⁷ interstellar chemistry,⁷⁸ organo metallic chemistry,⁷⁹ and planetary chemistry as presented at the present *Faraday Discussion*.^{80,81}

2.1.2. The crossed molecular beams machine. In case of reactions of dicarbon and methylidyne, the crossed molecular beam approach with universal mass-spectrometric detection presents the most versatile technique to study elementary reactions with reaction products of *unknown* spectroscopic properties. This helps to elucidate the chemical dynamics and – in the case of polyatomic reactions – the primary reaction products of bimolecular reactive encounters.⁸² The crossed beams machine consists of two source chambers at a crossing angle of 90°, a stainless steel scattering chamber, and an ultra-high-vacuum tight, rotatable, differentially pumped quadrupole mass spectrometric (QMS) detector which can be pumped down to a vacuum in the high 10⁻¹³ torr range.¹⁴ Multiple techniques can be applied to generate highly reactive beams. In the primary source, a *pulsed* beam of unstable (open shell) species are generated either by laser ablation (C, C₂, C₃),⁸³ laser ablation coupled with *in situ* reaction (CN, C₂D),⁸¹ photolysis (C₂H, C₂H₃, C₃H₃),⁸⁴ or flash pyrolysis (C₃H₅, C₆H₅).⁸⁵ The pulsed primary beam is passed through a skimmer into the main chamber; a chopper wheel located after the skimmer and prior to the collision center selects a part of the pulse with well-defined velocity which reaches the interaction region. This section of the beam then intersects a *pulsed* reactant beam released by a second pulsed valve under well-defined collision energies. The incorporation of *pulsed beams* allows reactions with often expensive (partially) deuterated and/or highly toxic chemicals to be carried out. Also, pulsed sources with high beam densities allow the pumping speed and hence cost to be reduced drastically.

To analyze the product(s), our machine incorporates a triply differentially pumped, *universal* quadrupole mass spectrometric detector coupled to an electron impact ionizer. Here, any reactively scattered species from the collision center after a single collision event has taken place can be ionized in the electron impact ionizer, and – in principle – it is possible to determine the mass (and the gross formula) of all

the products of a bimolecular reaction by varying the mass-to-charge ratio, m/z , in the mass filter. Since the detector is rotatable within the plane defined by both beams, this detector makes it possible to map out the angular (LAB) and velocity distributions of the scattered products. Measuring the time-of-flight (TOF) of the products, *i.e.* selecting a constant mass-to-charge value in the controller and measuring the flight time of the ionized species, from the interaction region over a finite flight distance at different laboratory angles allows extracting the product translational energy and angular distributions in the center-of-mass reference frame. This provides insight into the nature of the chemical reaction (direct *vs.* indirect), intermediates involved, the reaction product(s), their branching ratios, and in some cases the preferential rotational axis of the fragmenting complex(es) and the disposal of excess energy into the products' internal degrees of freedom as a function of scattering angle and collision energy. However, despite the triply differential pumping setup of the detector chambers, molecules desorbing from wall surfaces, which are on a straight line to the electron impact ionizer, cannot be avoided. Their mean free path is of the order of 10^3 m compared to maximum dimensions of the detector chamber of about 1 m. To reduce this background, a copper plate attached to a two-stage closed cycle helium refrigerator is placed right before the collision center and cooled down to 4 K. In this way, the ionizer views a cooled surface which traps all species with the exception of hydrogen and helium.

What information can we obtain from these measurements? The experimental observables contain some basic information. Every species can be ionized at the typical electron energy used in the ionizer and, therefore, it is possible to determine the mass and the gross formula of all the possible species produced from the reactions by simply selecting different m/z in the quadrupole mass spectrometer. Even though some problems such as dissociative ionization and background noise limit the method, the advantages with respect to spectroscopic techniques are obvious, since the applicability of the latter needs the knowledge of the optical properties of the products. In our setup, we are operating the ionizer during the scattering experiments at electron energies of 80 eV, *i.e.* at an energy at which the ionization cross section of the organic molecules is at their maxima.⁵⁶ Based on signal calculations, the crossed beam reactions of dicarbon and methylidyne radicals are very challenging and we need all the intensity (here: detectable ion counts) we can get. Note that our ionizer can be also operated *via soft* electron impact ionization as pioneered by Casavecchia *et al.*⁵⁸ This approach utilizes electrons with low, tunable energy (8–30 eV) to reduce strongly or even eliminate the problem of dissociative ionization from interfering species. However, soft ionization has – in case of the present experiments – one disadvantage: at electron energies of 8–30 eV, the ionization cross sections of the newly formed molecules are *at least* a factor of 20 lower than the electron impact ionization cross sections with 80 eV electrons.⁸⁶ Therefore, the low cross sections, the expected signal-to-noise, and the inherent data accumulation times make the application of soft ionization impractical for the present experiments utilizing *pulsed* beams. However, *soft electron impact ionization* and laser induced fluorescence (LIF) can be utilized to characterize the reactant beams on axis and *in situ* as described below. Another important aspect is that, by measuring the product velocity distributions, one can immediately derive the amount of the total energy available to the products and, therefore, the enthalpy of reaction of the reactive collision. This is of great help when different structural isomers with different enthalpies of formation can be produced. For a more detailed physical interpretation of the reaction mechanism it is necessary to transform the laboratory (LAB) data into the center-of-mass (CM) system using a forward-convolution routine.⁸⁷ This approach initially assumes an angular distribution $T(\theta)$ and a translational energy distribution $P(E_T)$ in the center-of-mass reference frame (CM). TOF spectra and the laboratory angular distribution are then calculated from these center-of-mass functions. The essential output of this process is the generation of a product flux contour map, $I(\theta, u) = P(u) \times T(\theta)$. This function reports the

flux of the reactively scattered products (I) as a function of the center-of-mass scattering angle (θ) and product velocity (u) and is called the reactive *differential cross section*. This map can be seen as the *image* of the chemical reaction and contains all the information on the scattering process.

2.1.3. The supersonic beam sources. *2.1.3.1. The ablation source: supersonic dicarbon beam.* Pulsed supersonic beams of dicarbon molecules are generated via laser ablation of graphite utilizing a home-built ablation source.⁸⁸ Here, a 266 nm laser beam originating from a neodymium-doped yttrium aluminium garnet (Nd:YAG) laser is tightly focused by a 1.5 m lens with pulse energies of 5–10 mJ onto a graphite rod performing a helical motion. The ablated species are seeded into helium carrier gas (99.9999%; Gaspro) at a backing pressure of 4 atm. Then, the supersonic beam of *in situ* generated dicarbon molecules is chopped and crosses a pulsed hydrogen cyanide beam (5% hydrogen cyanide premix in 99.9999% helium; Matheson Gas) perpendicularly in the interaction region at a collision energy of 42.4 ± 1.7 kJ mol⁻¹. Peak velocities of the dicarbon beam are 2019 ± 64 ms⁻¹ with a speed ratio of 4.2 ± 0.5 . The hydrogen cyanide beam segment crossing the dicarbon pulse is characterized by a peak velocity of 1612 ± 6 ms⁻¹ and speed ratio of 15 ± 3 . Note that the ablation beam also contains ground state carbon atoms (C(³P_g)). However, as demonstrated earlier in our group, atomic carbon does not react with hydrogen cyanide to form C₃N molecules plus atomic hydrogen at our collision energy.⁸⁹ Finally, the reaction of co-ablated tricarbon molecules with unsaturated bonds is hindered by entrance barriers larger than our collision energy.¹⁶ Also, we did not see reactive scattering signal at masses higher than $m/z = 50$. Therefore, the only species in the primary beam reacting with hydrogen cyanide are dicarbon molecules.

It is important to discuss the electronic states of the dicarbon molecules. Due to the low energy gap between the ground and first excited triplet state (718 cm⁻¹), the supersonic ablation beams contain dicarbon in its X¹Σ_g⁺ electronic ground state as well as in its first electronically excited a³Π_u state.⁹⁰ Crossed molecular beam reactions of dicarbon molecules with hydrogen sulfide (H₂S) and hydrogen cyanide (HCN) form the HCCS(X²Π_g)⁹¹ and CCCN(X²Σ⁺)²⁹ products *only* on the singlet surfaces. The corresponding reactions of triplet dicarbon are either repulsive (hydrogen sulfide reaction) or hold a significant entrance barrier of about 30 kJ mol⁻¹ (hydrogen cyanide). Therefore, those previous crossed beam reactions provided direct evidence that dicarbon molecules in their X¹Σ_g⁺ electronic ground state exist in the ablation beams. In order to verify the presence of triplet C₂ in the ablation beam we are conducting first a comprehensive laser induced fluorescence (LIF) study probing the dicarbon molecules in the first electronically excited state *via* the Swan transition (d³Π_g–a³Π_u). Here, triplet dicarbon was excited by the fundamental output of a Lambda Physics Scanmate dye laser using Coumarin 503 dye at about 516.5 nm at laser power of 45 μJ per pulse. The dye laser itself was pumped by an internal neodymium–yttrium–aluminium–garnet (Nd:YAG) laser operating at 355 nm at 10 Hz with an output power of 50 mJ per pulse. The dye laser was fired around 200 μs after the pulse valve opening with a pulse energy of a few μJ to intercept the peak of the dicarbon beam.⁹⁰ The geometry of the LIF detection experiment of triplet dicarbon is shown in Fig. 3 with the pulse sequence compiled in Fig. 4. The main experimental challenge of the LIF measurement was to suppress the scattered laser light in a tight volume of the crossed beams setup. To achieve this, the detection laser beam was focused to a 2–3 mm diameter spot at the crossing point by a 1.5 m lens. An antireflective coated lens has been employed to reduce multiple reflections in the lens that produce divergent beam components. A baffle tube containing eight irises of 4 mm and 5 mm diameter trapped divergent components in the detection laser beam. The skimmer of the secondary molecular beam has been removed to allow an unobstructed exit of the laser light. An ultra-low-backscatter laser beam trap (Thorlabs BT510, 6 × 10⁻⁶ fraction for integral

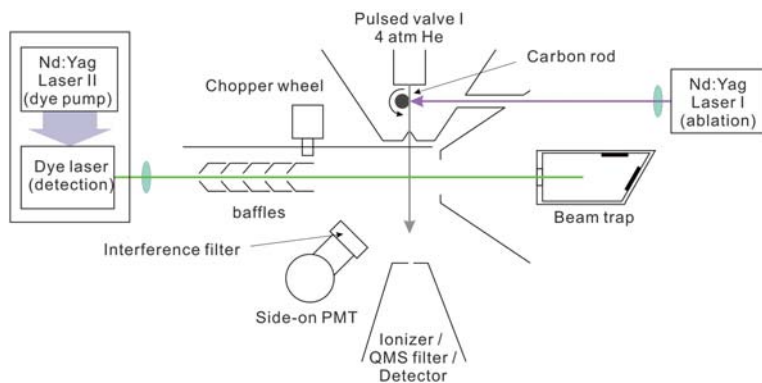


Fig. 3 Schematic geometry of the laser induced fluorescence (LIF) detection setup of triplet dicarbon as incorporated in the crossed beams machine.

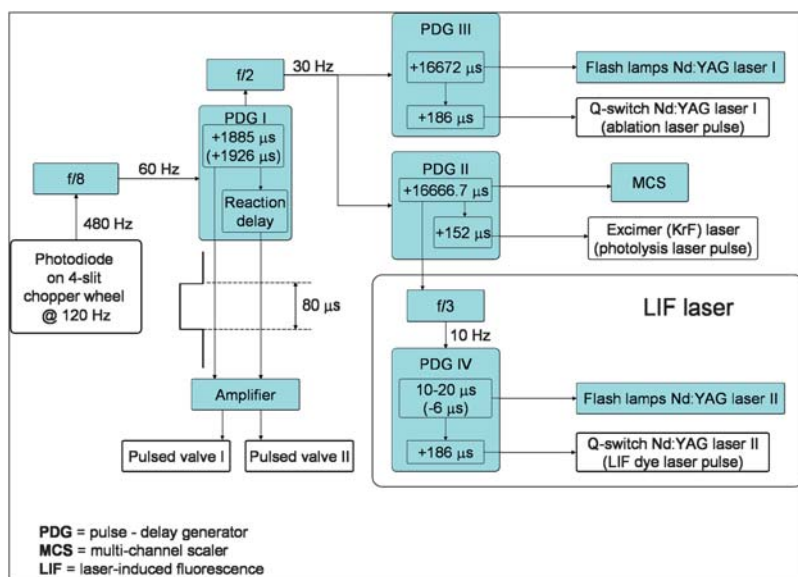


Fig. 4 Pulse sequence for the crossed beams experiments and LIF detection. Delay times are shown for distinct dicarbon beams produced in the primary chamber. For the methylidyne source, delay times different from the dicarbon experiment are shown in parentheses.

backscatter intensity) has been placed 50 cm behind the front wall of the secondary source to trap the detection beam. The fluorescence was detected by a Hamamatsu R955 photomultiplier tube (PMT) placed between the baffle tube and the detector chamber at about 10 cm from the intersection point. A band pass interference filter of 10 nm bandwidth centered at 562 nm (Andover) was placed in front of the PMT to block the scattered laser light and to pass the fluorescence to the first vibrationally excited ground electronic states of dicarbon. No spatial filtering of collected light was introduced. The signal was amplified by a built in preamplifier of the Hamamatsu C7247 PMT socket assembly prior to feeding into a digital oscilloscope and a computer for data collecting and processing. The LIF spectra were then analyzed utilizing the diatomic spectral simulation program by Tan⁹² with spectroscopic constants from Bernath.⁹³ The corresponding LIF spectra of dicarbon seeded

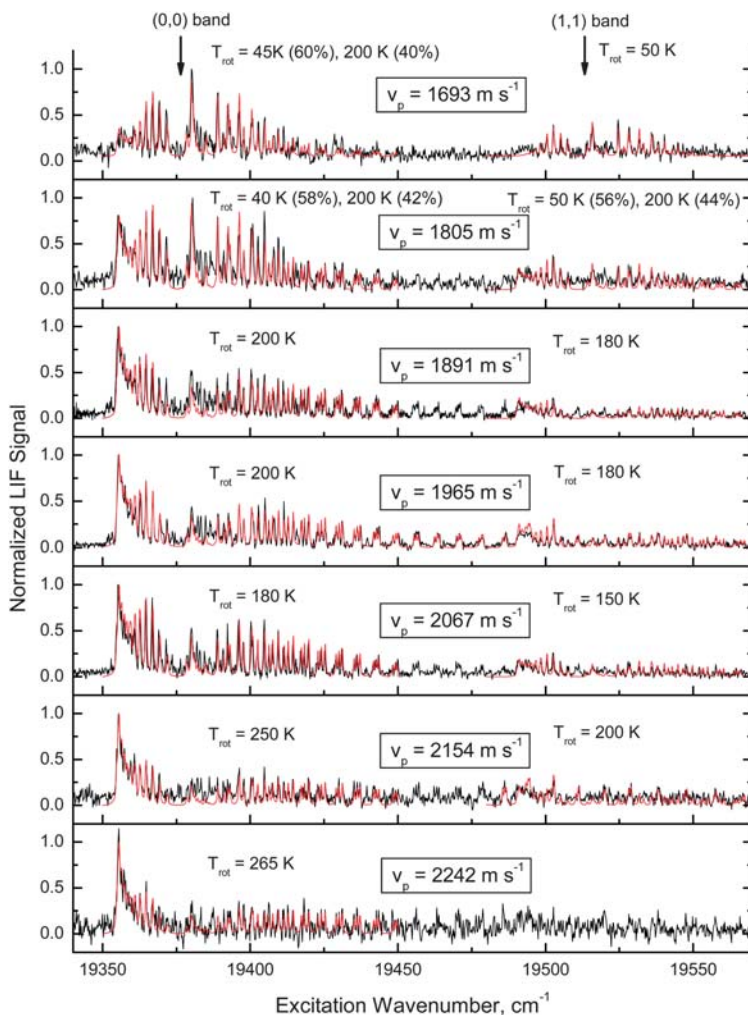


Fig. 5 LIF excitation spectra of dicarbon seeded in helium carrier gas for different velocities of the beam. Temperatures of the best-fit for rotational energy distributions are listed separately for the (0,0) and (1,1) bands. Some distributions have distinct non-equilibrium character; they are fit with two temperature components.

in helium and neon carrier gases are shown in Fig. 5 and 6, respectively. Different peak velocities (v_p) of the beam were chosen by selecting distinct delay times between the pulsed valve and the chopper wheel. The peaks in the spectra correspond to the excitation from different rotational states of the ground vibrational state of triplet dicarbon ((0,0) band) and of the first excited vibrational state ((1,1) band). Vibrational (0,0) and (1,1) bands are separated on the energy scale. Their integral intensity ratio is determined by the relative populations of the $\nu = 0$ and $\nu = 1$ states. We did not observe transitions from vibrational states higher than $\nu = 1$.

Fig. 7 addresses the dependence of the vibrational and rotational temperatures as well as speed ratios on the peak velocities of distinct parts of the chopped dicarbon beam. The vibrational temperature is expressed in practical terms of the fraction of triplet dicarbon in $\nu = 1$. The majority of the LIF spectra can be fitted well if we treat the vibrational and rotational temperatures for each vibrational state separately. In some spectra, however, we have to introduce two temperatures and a bimodal

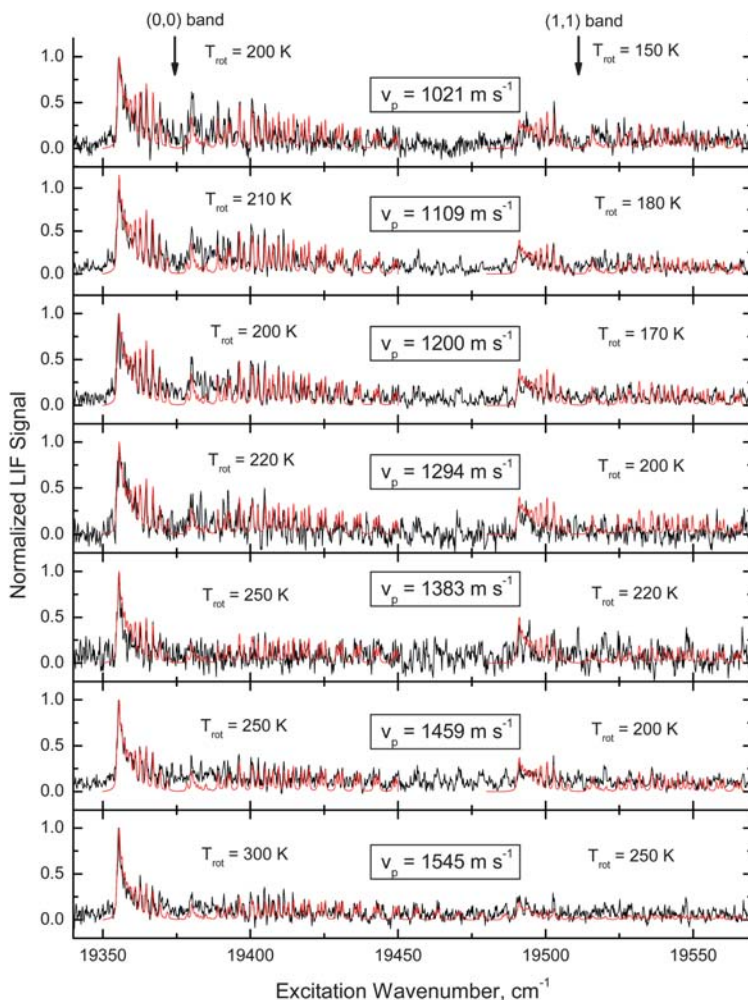


Fig. 6 LIF excitation spectra of dicarbon seeded in neon carrier gas for different velocities of the beam. Temperatures of the best-fit for rotational energy distributions are listed separately for the (0,0) and (1,1) bands.

distribution to describe the distribution of rotational state populations within one vibrational state. This probably indicates highly non-equilibrium energy distribution in the dicarbon molecules following graphite laser ablation events. The general trend for the speed ratio and the rotational temperature is that lower velocities provide cooler molecules; rotational temperatures as low as 50 K can be achieved. This is consistent with the fact that the ablated species seeded in the fast (front) parts of the helium and neon pulses have less collisions with the noble gas causing lower cooling efficiency. Rotational temperatures for $\nu = 1$ are systematically lower than for $\nu = 0$ suggesting a better rotational cooling of vibrationally excited species. There are some irregularities in the velocity dependence of the beam characteristics; these can be partially attributed to variations in the independently adjusted delay times of the pulsed valve and ablation laser as well as slight variations in the ablation laser power leading to distinct seeding conditions. Also, the vibrational population dependence on velocity does not exhibit a pronounced trend. Vibrational relaxation is about equally inefficient in the whole range of experimental conditions.

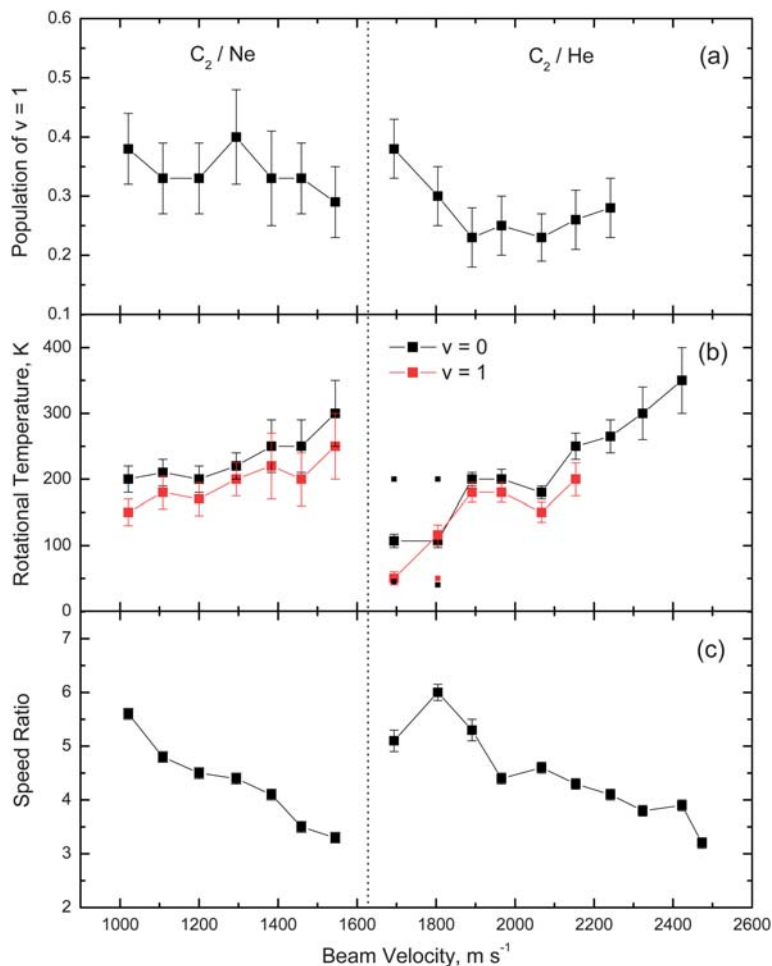


Fig. 7 Supersonic vibrational (a), rotational (b), and speed ratio (c) dependence on the dicarbon beam peak velocity. The dicarbon molecules are seeded in neon (left part) and helium (right part) carrier gases. The cooling efficiency is characterized in terms of the population of the first vibrationally excited state (a), rotational temperature (b), and speed ratio of the beam (c). Black and red curves in (b) represent rotational temperatures of $\nu = 0$ and $\nu = 1$, respectively. The smaller squares plot temperature components of a non-equilibrium energy distribution.

As compiled in Fig. 4, the 17 cm diameter four-slit chopper wheel with 0.76 mm slits operates at 120 Hz between the skimmer of the primary source and the interaction region. An infrared diode attached to the top of the chopper unit detects the slit passage thus providing the time zero of the experiment. By selecting the time delay between the diode pulse and the pulsed valve, distinct parts of the ablation pulse can be selected. An SRS DG535 delay/pulse generator (PDG I) is triggered at 60 Hz by the frequency divided output of the diode. The two outputs, AB and CD, of the pulse generator (50 Ω , +3.5 V, 80 μ s pulse width) lead to a homemade pulse shaper, which in turn is connected to the Physik Instrumente P-286.23 high voltage pulse amplifier. The output of the amplifier drives both piezoelectric Proch-Trickl valves at repetition rates of 60 Hz, opening times of 80 μ s, and pulse amplitude of minus 400 V to 500 V. The delay time between the two valves provides for simultaneous arrival of the most intensive parts of the two reactant beams to the interaction region. The A output of the PDGI pulse generator (TTL, high impedance) passes

a frequency divider (division by two, 50 Ω output) fed as an external trigger to a second delay/pulse generator (PDG II). The time delayed A output ($A = T_0 + 16\,666.66\ \mu\text{s}$, high impedance TTL) is fed into the SRS 430 multichannel scaler (MCS) utilizing trigger and discriminator levels of +0.5 and +0.2 V. A second output of the frequency divider serves as an external trigger of PDG III. This unit controls the time sequence of Spectra Physics Nd:YAG laser (30 Hz, 120 mJ per pulse at 266 nm). Channel AB ($A = T_0 + 16,672\ \mu\text{s}$, $B = A + 5\ \mu\text{s}$, 50 Ω , TTL) triggers the flash lamps and CD the Q-switch ($C = A + 186\ \mu\text{s}$, $D = C + 5\ \mu\text{s}$, 50 Ω , TTL). The time sequence for Nd:YAG pumped dye laser (10 Hz repetition rate) used for LIF detection is set by PDG IV triggered by the frequency divided A output of PDG II. Channel AB ($A = T_0 + (10\text{--}20)\ \mu\text{s}$, $B = A + 5\ \mu\text{s}$, 50 Ω , TTL) triggers the flash lamps and CD the Q-switch ($C = A + 186\ \mu\text{s}$, $D = C + 5\ \mu\text{s}$, 50 Ω , TTL) of the internal Nd:YAG laser. Delays for the primary pulsed valve and ablation laser were varied slightly depending on desired velocity of the dicarbon beam.

2.1.3.2. The photolytic source: supersonic methylidyne beam. We generated a pulsed supersonic beam of methylidyne radicals *via* photolysis of helium-seeded bromoform (CHBr_3) at seeding fractions of 0.12% at 248 nm at 30 Hz by bubbling helium gas (99.9999%; Gaspro) at a pressure of 2.2 atm through a stainless steel bubbler which houses the bromoform at a temperature of 283 K and feeding this gas mixture into a pulsed piezoelectric valve. The latter is operated at a repetition rate of 60 Hz, pulse widths of 80 μs , and a voltage of minus 400 V to 450 V. Here, by focusing 60 mJ per pulse output of excimer laser (KrF) with a 1 meter focus lens downstream of the nozzle to an area of about 4 mm by 0.7 mm, a few 10^{12} radicals cm^{-3} can be formed in the interaction region of the scattering chamber. The timing of the experiment is shown in Fig. 4 alongside with the timing for the dicarbon experiment. If the delay times differ, the values for the methylidyne experiment are shown in parentheses.

Methylidyne radicals are only produced in the $^2\Pi$ ground state. The A and B states have lifetimes of $440 \pm 20\ \text{ns}$ and $470 \pm 20\ \text{ns}$ and relax to the ground state before they reach the skimmer.⁹⁴ The photodissociation of bromoform to $\text{CH}(X^2\Pi)$ is a multiphoton process initiated by the cleavage of the C–Br bond to yield $\text{CHBr}_2 + \text{Br}^{95}$ ($\sigma(248\ \text{nm}) = 1.9 \times 10^{-18}\ \text{cm}^2$).⁹⁶ Utilizing photoionization photofragment translational spectroscopy, North *et al.* observed also CHBr , CBr , HBr , and Br_2 fragments which were attributed to higher-order photodissociation processes of CHBr_2 and CHBr . Mebel computed the photodissociation cross sections of CHBr_2 and CHBr at 248 nm to be $1.6 \pm 0.4 \times 10^{-18}$ and $2.0 \pm 0.3 \times 10^{-18}\ \text{cm}^2$, respectively.⁹⁷ Although it is not feasible to eliminate CHBr_2 , CHBr , and CBr in the supersonic beam, these molecules have – due to the heavy bromine atom – distinct center-of-mass angles when reacting with the hydrocarbon molecules. Therefore, the dynamics can be distinguished from those of the CH reactions based on the distinct mass-to-charge ratios and due to different center-of-mass angles and hence scattering ranges of the products. This presents a unique advantage of the present experimental setup. The velocity and speed ratio of the radical beam can be determined on-axis in the TOF mode. Since signal at $m/z = 13$ (CH^+) also originates from dissociative ionization of, for instance, non-photolyzed bromoform, operating the electron impact ionizer in the *soft ionization* mode, here at 34 eV, for the beam characterization is important. This translates into a narrow range of peak velocities of 1680–1780 ms^{-1} with speed ratios of 12–18.

We also utilized laser induced fluorescence to characterize the rotational and vibrational modes of the methylidyne radical, $\text{CH}(X^2\Pi)$, in the interaction region of the scattering chamber. Methylidyne radicals are detected using $A^2\Delta\text{--}X^2\Pi$ transitions: (0,0) vibrational band for excitation near 431 nm and (0,1) band for detection near 490 nm. The interference filter in front of the photomultiplier tube (PMT; Andover Corp.) is centered at 490 nm with a 10 nm bandwidth; this discriminates against scattered laser light. Two major modifications have been made to LIF detection setup compared to dicarbon experiment (Fig. 3). Firstly, the skimmer of the

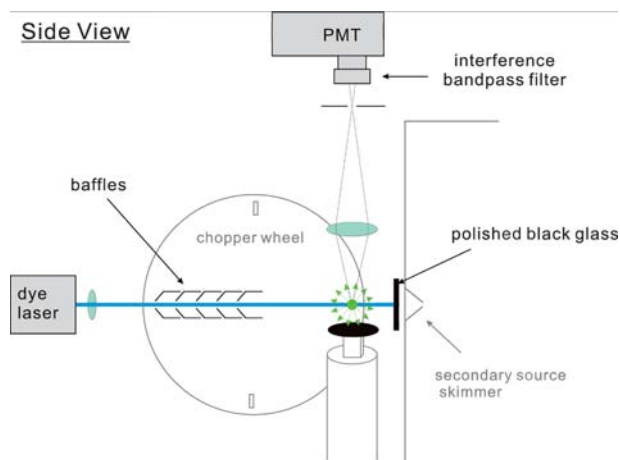


Fig. 8 Schematic geometry of the laser induced fluorescence detection setup of the methylidyne radical as incorporated in the crossed beams machine.

secondary source does not have to be removed in the new configuration (Fig. 8). The incoming detection laser beam is mainly absorbed by a piece of polished black glass (ThorLabs; neutral density filter; 40–20 surface quality); the reflected part travels back into the baffle tube. Secondly, spatial filtering of fluorescence signal is introduced. The fluorescence spot in the interaction region is projected by a 35 mm focus lens onto the center of the iris in front of the PMT, which is mounted on the lid of the machine. This vertical orientation of the detector allows also us to minimize the collection of Rayleigh scattered light of the vertically polarized laser on the atoms and molecules in the beam. Another piece of polished black glass is placed under the interaction region to eliminate the propagation of scattered laser light in the light

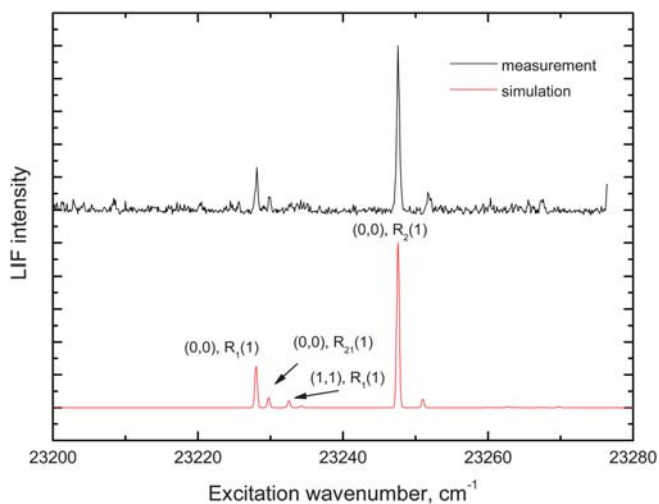


Fig. 9 LIF spectrum of helium-seeded methylidyne radicals (top) together with the simulation. Parameters of the best fit simulation suggest a rotational temperature of 14 K and relative populations of $\nu = 1$ level of less than 6% based on the (1,1), $R_1(1)$ peak. Note that we cannot distinguish between different spin–orbit states of methylidyne radical ($\Omega = 1/2$ vs. $\Omega = 3/2$) because for the observed transitions, the largest spectroscopic splitting (0.11 cm^{-1} for $R_2(1)$ transition) would be still smaller than the line width of the detection laser of 0.15 cm^{-1} .

collection cone. Fig. 9 shows the LIF spectrum of the methylidyne radical beam with a peak velocity of 1700 ms^{-1} as characterized with the TOF technique. Sixteen detection laser shots were averaged for each point. The spectrum was analyzed utilizing a LIFBASE database and spectral simulation for diatomic molecules by Jorge Luque.⁹⁸ The best fit simulation suggests a rotational temperature of $14 \pm 1 \text{ K}$ in the vibrational ground state; less than 6% of the radicals are in the first vibrationally excited state population. We conducted two test reactions of this beam by crossing it with argon-seeded diacetylene (C_4H_2) and neat methylacetylene (C_3H_4). The diacetylene beam has a peak velocity of $600 \pm 15 \text{ ms}^{-1}$ at a speed ratio of 8; the neat methylacetylene beam was characterized by a velocity of $840 \pm 10 \text{ ms}^{-1}$ and a speed ratio of 9.

2.2. The surface scattering machine

A surface scattering machine, in which an ultrahigh vacuum in the low 10^{-11} torr range can be achieved (Fig. 10),⁹⁹ was utilized to simulate the interaction of energetic electrons with organics as present on Titan in form of aerosol ‘droplets’ and solids on Titan’s surface. Ethane (C_2H_6) and propane (C_3H_8) ices were prepared in separate experiments by passing ethane (99.999%; Gaspro) and propane (99.9%; Specialty Gas Group) for 3 min through a glass capillary array at hydrocarbon pressures of 1.5×10^{-8} Torr onto a highly polished silver mono-crystal. The silver substrate is attached to the freely rotating arm of a closed cycle helium refrigerator (CTI-Cryogenics CP-1020) and was held at $11.3 \pm 0.5 \text{ K}$ to allow for the rapid condensation of the gases. The temperature of the ice samples was measured by a silicon diode connected to a Lakeshore 331 temperature controller. Recall that Titan’s surface temperature of 94 K is well above the 11.3 K of the cold head. Therefore, the ices were heated to 50 K (C_2H_6) and 65 K (C_3H_8) – just before the sublimation temperature under UHV conditions – and then irradiated with 5 keV electrons supplied by an electron gun (SPECS EQ 22) for 3 h at a beam current of 500 nA. The manufacturer states an electron extraction efficiency of 78.8%; this resulted in an exposure of 1.5×10^{16} electrons per cm^2 over the irradiation time with an irradiation area of $1.8 \pm 0.3 \text{ cm}^2$. The analysis of the irradiated ice samples was performed on line and *in situ* with a Nicolet 6700 FTIR spectrometer operating in absorption–reflection–absorption mode (reflection angle $\alpha = 75^\circ$) to the surface. Spectra were recorded at a resolution of 2 cm^{-1} over the mid-IR ranges

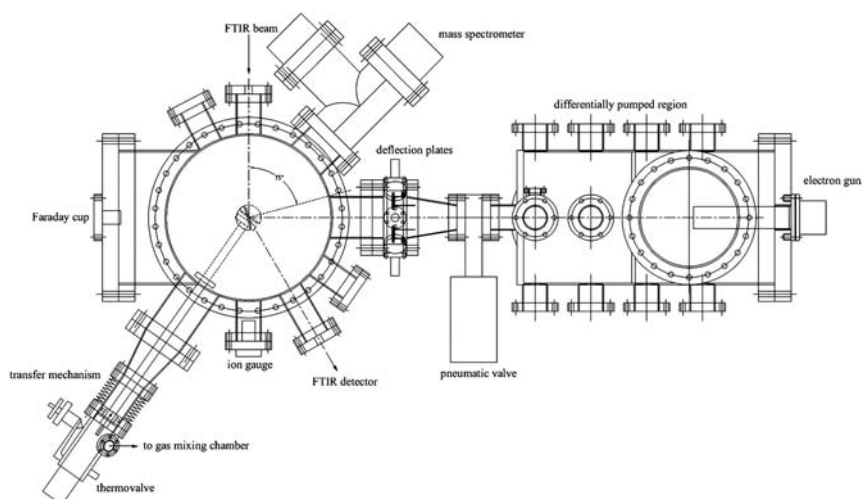


Fig. 10 Schematic top view of the surface scattering machine.⁹⁹

(4000–500 cm^{-1}) utilizing a liquid nitrogen cooled mercury–cadmium–telluride detector. Gaseous species were monitored by a Balzer QMG 420 QMS operating in residual gas analyzer mode with an electron impact ionization energy of 100 eV and a mass range of up to 200 amu. Upon completion of the irradiation period, the ice samples were then heated to 300 K by a controlled heating program at a rate of 0.5 K per minute to allow for the analysis of volatile products as they sublimed from the target.

The analysis of the infrared bands of pristine ethane (C_2H_6) and propane (C_3H_8) allowed for the calculation of the thickness of the deposited ice layers using the integral absorption coefficients for the methyl group (CH_3) deformation bands provided by Bohn *et al.*¹⁰⁰ and the densities of ethane ($0.713 \pm 0.002 \text{ g cm}^{-3}$) and propane ($0.763 \pm 0.004 \text{ g cm}^{-3}$) at 77 K as given in Stewart and La Rock.¹⁰¹ The thicknesses were calculated to be $200 \pm 50 \text{ nm}$ for ethane (C_2H_6) and $180 \pm 30 \text{ nm}$ for propane (C_3H_8). To gain a quantitative handle on the energy absorbed by the hydrocarbon molecules, the electron trajectories in the ice samples and the energy transfer were then simulated by the CASINO code.¹⁰² This code calculates average transmission energies of the energetic electrons of $4.56 \pm 0.01 \text{ keV}$ and $4.59 \pm 0.01 \text{ keV}$ for ethane and propane ices, respectively. Therefore, each electron deposits on average $440 \pm 10 \text{ eV}$ into the ethane sample (linear energy transfer $\text{LET} = 3.7 \pm 0.2 \text{ keV } \mu\text{m}^{-1}$) and $410 \pm 10 \text{ eV}$ into the propane ice ($\text{LET} = 3.7 \pm 0.4 \text{ keV } \mu\text{m}^{-1}$). From here, the average amount of energy absorbed per target molecule, the dose, is calculated to be 36 ± 2 and $53 \pm 5 \text{ eV}$ per molecule for the ethane and propane samples.

2.3. The laser ablation apparatus

The experiments were performed with a laser ablation apparatus coupled to a 3 meter monochromator of the Chemical Dynamics Beamline at the Advanced Light Source.¹⁰³ The apparatus was described previously.¹⁰⁴ Compared to the original design, the ablation source was modified to incorporate an external motor assembly as described below (Fig. 11). Briefly, the ablation source consists of an aluminium block and a pulsed piezoelectric valve. The 6.35 mm diameter silicon rod (ESPI) rotates and simultaneously translates vertically inside of the aluminium ablation block, which acts as a guide for the ablation rod. The latter is connected to an in-vacuum translation-rotation stage, which is driven by a computer controlled stepper motor (RMS technologies) connected through a speed reducing gear box. A frequency doubled (532 nm) Nd:YAG laser operating at 50 Hz and output powers of about 0.8 mJ per pulse ablates the silicon rod. The ablated species are entrained in acetylene (C_2H_2 ; Airgas) carrier gas released by a Proch–Trickl piezo valve. Acetone, which acts as a stabilizer in the pressurized acetylene cylinder, is filtered out before the gas enters the piezo valve at a stagnation pressure of 1.5 atm. The ablated silicon-bearing species travel together with the gas pulse inside a 4 mm diameter 30 mm long extension channel before exiting the ablation block. The acetylene acts both as a carrier gas and as a reagent media; therefore, the organo-silicon molecules are formed *in situ* in the supersonic beam *via* reaction of acetylene with the ablated silicon species. This technique has been applied recently to produce and to derive the ionization energies of highly reactive organic transient radicals like linear and cyclic C_3H radicals.¹⁰⁵ A pair of deflection plates, producing an electrical field of about 660 V cm^{-1} , are located between the ablation block and skimmer assembly thus removing charged species generated by the ablation process; this allows only neutral particles to pass through the differential pumping wall, which is equipped with a 2 mm skimmer hole; this section separates the source chamber from the main photoionization chamber.

The neutral, supersonic beam is interrogated in the ionization region of a commercially available reflectron time-of-flight mass spectrometer (R. M. Jordan) by tunable monochromatic synchrotron radiation in the vacuum ultraviolet (VUV) region of the electromagnetic spectrum. Typically $10^{13} \text{ photons s}^{-1}$ are available at

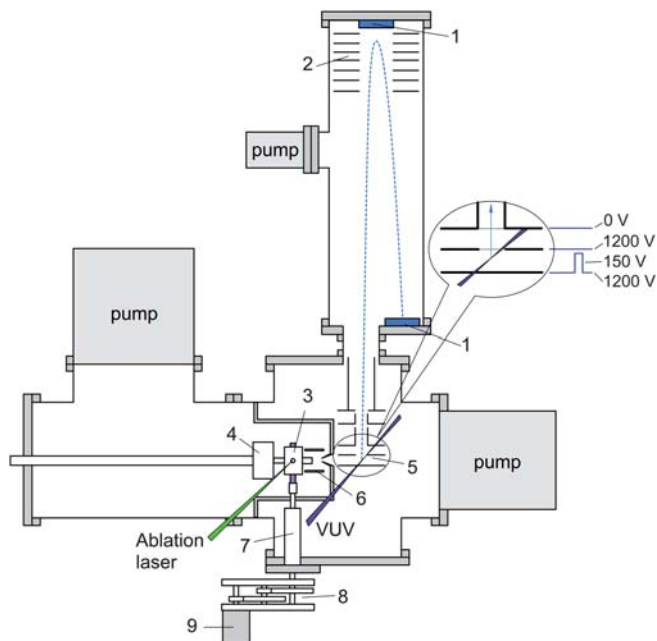


Fig. 11 Scheme of the laser ablation setup machine: 1) micro-channel plates, 2) reflectron, 3) ablation block with a silicon rod, 4) pulsed piezo valve, 5) Wiley-McLaren ion optics, 6) ion deflection plates, 7) translation-rotation stage, 8) gear box, 9) step motor.

this terminal. The photoionization region is situated 12 cm downstream from the ablation region. As the synchrotron light is quasi-continuous (500 MHz), a start pulse for the time-of-flight (TOF) ion packet is provided by pulsing the repeller plate (the lowest electrode in the Wiley-McLaren ion optics) of the time-of-flight ion optics. The pulsing sequence with voltages are shown in the inset of Fig. 11. The ions hit a microchannel plate (MCP) detector; the signal from these ions are collected with a multichannel-scalar card (FAST Comtec 7886) triggered by the repeller plate pulse. Time-of flight spectra, *i.e.* the flight time of the ion *versus* the intensity of the ion counts, are recorded for the photoionization energy range between 8.0 eV and 10.5 eV. The typical step size used for these experiments is 50 meV; the signal was collected for $5\text{--}7 \times 10^3$ laser shots. The detected signal was optimized using LabView (National Instruments) routines by changing the delay times (Nd:YAG lamp to Q-switch to attenuate laser pulse intensity; laser pulse to trigger pulse to piezo valve; laser pulse to repeller plate pulse) and voltages of the TOF ion optics.¹⁰⁴ Previously, we estimated that typically $10^8\text{--}10^9$ molecules cm^{-3} are being ionized in the 1 mm^3 interaction region.

The photoionization efficiency (PIE) curves of a well-defined ion of a mass-to-charge ratio (m/z) can be obtained by plotting the integrated ion signal at the mass-to-charge *versus* the photoionization energy between 8.0 eV and 10.5 eV, normalized by the photon flux and the number of laser shots. The synchrotron VUV photon flux is measured by a Si photodiode (IRD, SXUV-100). These PIE curves can be exploited to extract the adiabatic ionization energies of the newly formed silicon bearing species. To calibrate the photon energy, auto ionization peaks of xenon and a resonance feature in the PIE curve of atomic silicon are used. Thus, to measure the energy resolution of the VUV light, scans of a resonance in the PIE spectrum of atomic silicon due to its atomic transitions were undertaken. The resulting PIE curves were measured in the photon energy range from 9.82 eV to 9.93 eV for three different sizes of the 3 meter monochromator exit slits; these are

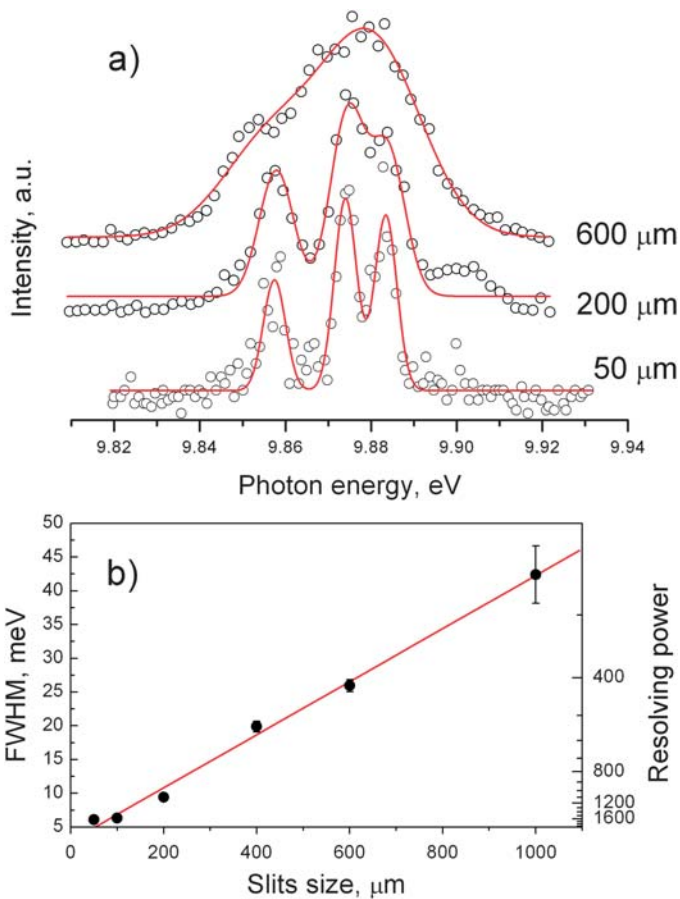


Fig. 12 a) Resonance features in the photoionization efficiency curves of atomic silicon for 50 μm, 200 μm, and 600 μm monochromator exit slits; b) the dependence of the full width at half maximum (FWHM) of the synchrotron VUV radiation and its resolving power on the monochromator exit slit size.

shown in Fig. 12 and are fitted with a Gaussian function. It is observed that the energy resolving power ($E/\Delta E$) is 1650 for 50 μm slits; this degrades to 250 for a slit width of 1 mm.

3. Theoretical approach

Molecular geometries and vibrational frequencies of reactants, intermediates, and transition states on the potential energy surface of the reaction of hydrogen cyanide (HCN) with triplet dicarbon ($C_2(^3\Pi_u)$) were calculated at the hybrid density functional B3LYP/6-311G** level of theory¹⁰⁶ using the GAUSSIAN 98 program package.¹⁰⁷ Relative energies were refined utilizing the coupled cluster CCSD(T) method as implemented in the MOLPRO package¹⁰⁸ with extrapolation to the complete basis set (CBS) limit. To achieve this, we computed CCSD(T) total energies for each stationary point with Dunning's correlation-consistent cc-pVDZ, cc-pVTZ, cc-pVQZ, and cc-pV5Z basis sets and projected them to CCSD(T)/CBS total energies using eqn (8):

$$E_{\text{tot}}(x) = E_{\text{tot}}(\infty) + Be^{-Cx} \quad (8)$$

where x is the cardinal number of the basis set (2, 3, 4, and 5) and $E_{\text{tot}}(\infty)$ is the CCSD(T)/CBS total energy. With respect to calculations of the organo silicon neutral molecules and ions, we used the same B3LYP/6-311G** approach for the geometry optimization and evaluation of vibrational frequencies. Relative energies of various isomers as well as vertical and adiabatic ionization energies were then refined by single-point energy calculations at the CCSD(T)/cc-pVQZ level of theory.

4. Results & discussion

4.1. Crossed beam reactions

In our experiments of dicarbon with hydrogen cyanide, we recorded time-of-flight (TOF) spectra at various laboratory angles at mass to charge ratios of $m/z = 50$ (C_3N^+) and higher. Similar to the reactions of ground state singlet dicarbon conducted previously in our group at collision energies of 22.4 kJ mol^{-1} and of 25.8 kJ mol^{-1} ²⁹ we detected signal at mass to charge ratios $m/z = 50$ (C_3N^+) (Fig. 13). Also, we could confirm that even at a collision energy of 42.4 kJ mol^{-1} , no products at higher masses were monitored. It is important to stress that all TOF spectra were fit with a single channel leading to the synthesis of a molecule of the gross formula C_3N formed through a dicarbon molecule *versus* hydrogen atom exchange; the formation of the thermodynamically less stable isocyano radical (CCNC) is endoergic by 102 kJ mol^{-1} and hence can be ruled out considering our collision energy of only 42.4 kJ mol^{-1} . Consequently, we propose that the cyanoethynyl radical (CCCN) is also the reaction product at $m/z = 50$. Note that the corresponding laboratory angular distribution is very narrow and spread only 30° in the scattering plane as defined by the dicarbon and hydrogen cyanide beams. Therefore, we can conclude that both in the previous reactions of singlet dicarbon and now with singlet and triplet dicarbon, the cyanoethynyl radical can be formed under single collision conditions.

Having analyzed the laboratory data, we now focus our attention to the derived center-of-mass functions. As outlined before, an acceptable fit could be achieved with a single reaction channel. Here, a close look at the center-of-mass translational

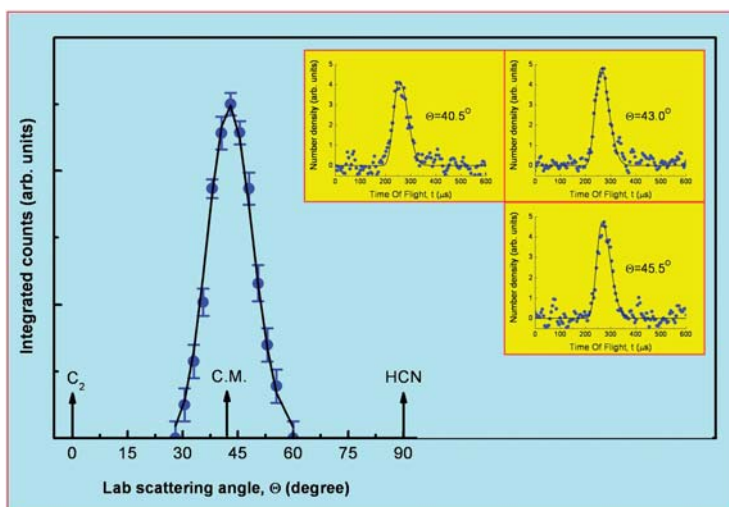


Fig. 13 Laboratory angular distribution and selected time-of-flight (TOF) spectra of the C_3N radical, which was formed in the reaction of dicarbon with hydrogen cyanide, recorded at $m/z = 50$ at a collision energy of 42.4 kJ mol^{-1} utilizing a single channel fit with the center-of-mass functions as shown in Fig. 14.

energy distribution (Fig. 14) assists to compare the experimentally derived reaction energy with theoretically predicted value. By subtracting the collision energy (E_C) of 42.4 kJ mol^{-1} from the maximum translational energy released into the translational degrees of freedom of the reaction products, here $60 \pm 5 \text{ kJ mol}^{-1}$, the reaction was found to be exoergic by $18 \pm 10 \text{ kJ mol}^{-1}$. This data is in good agreement with our *ab initio* data of $21 \pm 5 \text{ kJ mol}^{-1}$ for the triplet dicarbon reaction. Secondly, the translational energy distribution shows a plateau ranging from about 12 to 20 kJ mol^{-1} . As found from previous reactions of singlet and triplet dicarbon with acetylene and ethylene, these patterns could suggest the existence of two reaction pathways on the singlet and on the triplet surface. Recall that the translational energy distribution obtained at lower collision energies of 22.4 kJ mol^{-1} and of 25.8 kJ mol^{-1} , *i.e.* only from the singlet dicarbon reaction, peaked at zero translational energy, suggesting a barrierless decomposition of an intermediate – in this case singlet

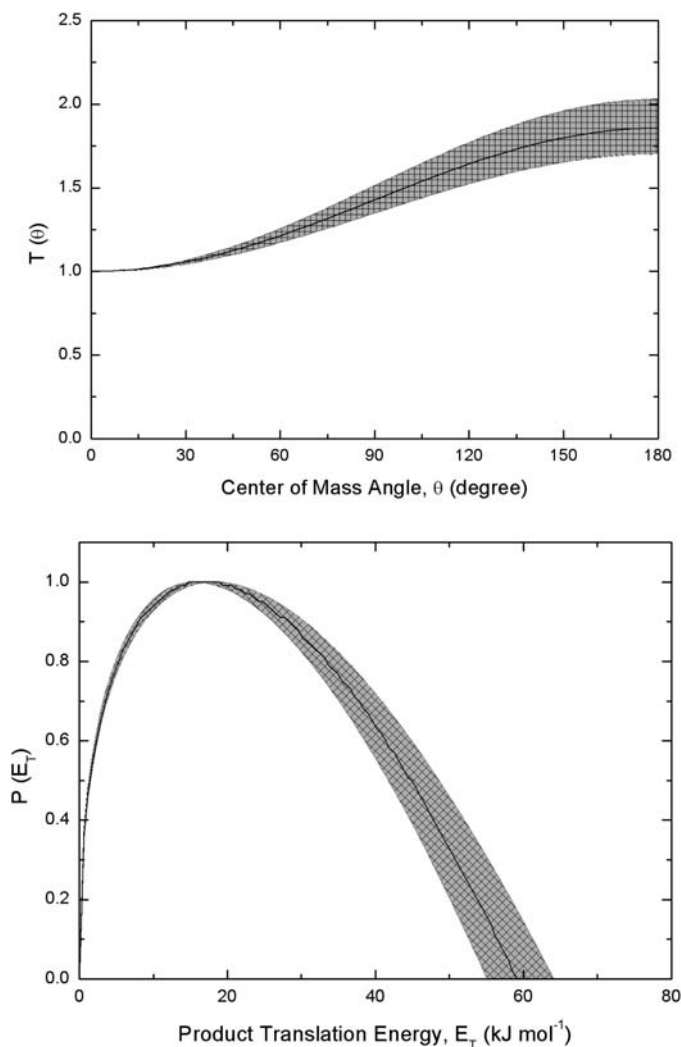


Fig. 14 Center-of-mass angular (top) and translational energy distributions (bottom) of the C_3N radical plus atomic hydrogen channel open in the reaction of dicarbon with hydrogen cyanide; the collision energy of the experiment was 42.4 kJ mol^{-1} .

cianoacetylene – to form atomic hydrogen and the CCCN radical. However, in case of Fig. 14 and the involvement from channels on the singlet and triplet surface, we can therefore propose that the triplet surface should involve a reaction intermediate which decomposes *via* a rather tight exit transition state. Further, the center-of-mass angular distribution (Fig. 14) depicts intensity over the complete scattering range from $\theta = 0^\circ$ to $\theta = 180^\circ$. This pattern is indicative of the involvement of reaction intermediates. Most intriguing, at both lower collision energies of 22.4 kJ mol^{-1} and of 25.8 kJ mol^{-1} , in which only singlet dicarbon reacted, the authors observed a forward-scattered distribution with the intensity in the forward hemisphere increasing as the collision energy rose. Therefore, if only the singlet channel reacted at an even higher collision energy of 42.4 kJ mol^{-1} as in the present experiment, we would predict an even greater forward-peaking of the center-of-mass angular distribution (typical osculating complex model if only one reaction channel and one decomposing intermediate, here cyanoacetylene HC_3N , is involved). However, this is clearly not observed. Therefore, the backward scattering is likely attributable to the involvement of the reactions of triplet dicarbon.

Having unraveled that both the singlet and the triplet dicarbon molecules lead to distinct scattering dynamics of an osculating complex (singlet surface) and a backward-scattering (triplet surface), we are now refitting the laboratory data and superimpose a two channel fit for the singlet and triplet channel separately in an attempt to untangle the contribution of singlet *versus* triplet dicarbon to the reactive scattering signal. Again, it must be stressed that we could also fit the data of $m/z = 50$ with a single channel; the separation of the single center of mass function into two is carried out because we have explicit evidence of the reaction on the singlet and triplet surfaces. The results of this procedure are shown in Fig. 15 and 16. Here, the TOF spectra and the laboratory angular distribution can be fit with two reaction channels accounting for singlet and triplet dicarbon with relative weighting factors of about one to six. Assuming a similar reaction cross section, this demonstrates that dicarbon in its first excited triplet state is much more abundant in the ablation beam at a collision energy of 42.4 kJ mol^{-1} compared to singlet dicarbon. On the singlet surface, the center-of-mass translational energy distribution is

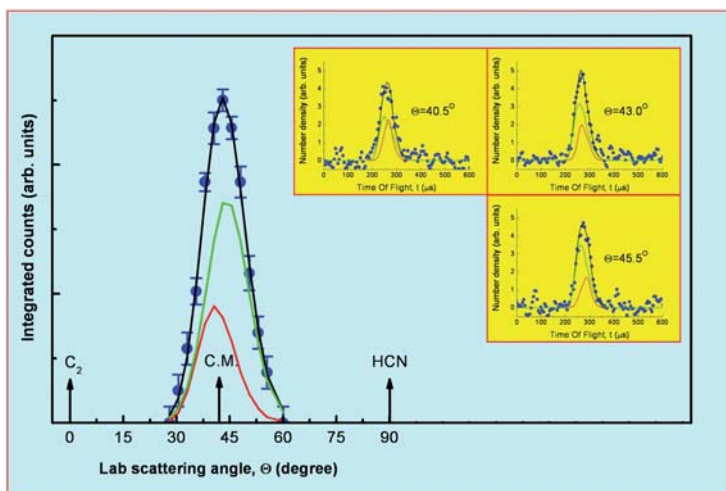


Fig. 15 Laboratory angular distribution and selected time-of-flight (TOF) spectra of the C_3N radical, which was formed in the reaction of dicarbon with hydrogen cyanide, recorded at $m/z = 50$ at a collision energy of 42.4 kJ mol^{-1} utilizing a two-channel fit with the center-of-mass functions as shown in Fig. 16; red: singlet channel; green: triplet channel.

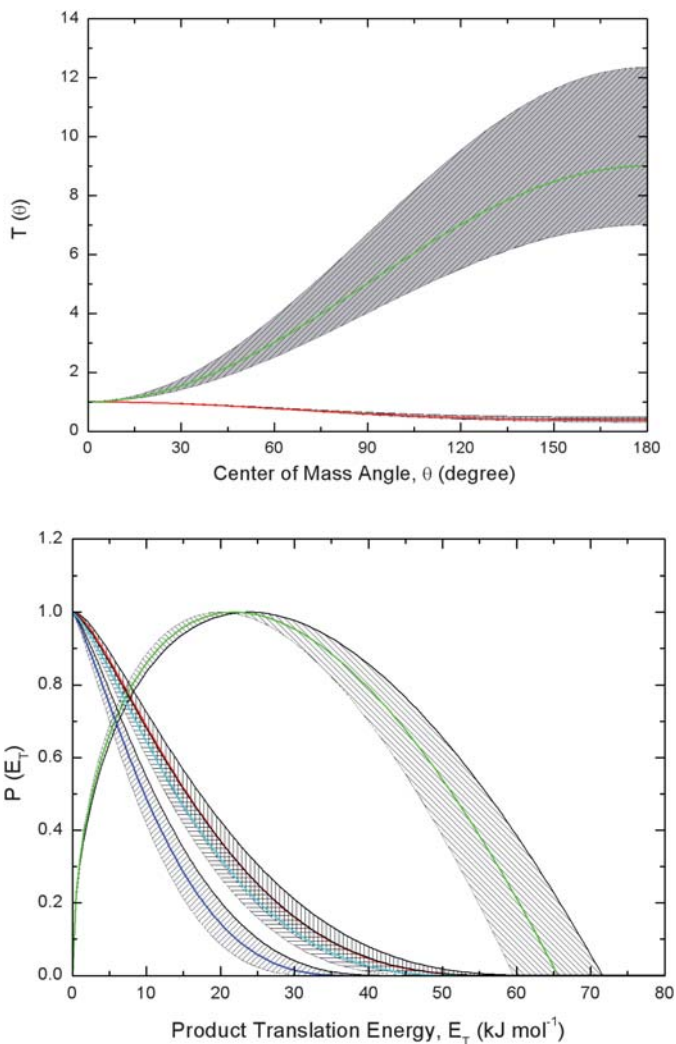


Fig. 16 Center-of-mass angular (top) and translational energy distributions (bottom) of the C_3N radical plus atomic hydrogen channel open in the reaction of dicarbon with hydrogen cyanide; the collision energy was 42.4 kJ mol^{-1} . For this two channel fit, green corresponds to the triplet and red to the singlet channel. For comparison, translational energy distribution extracted from experiments at 22.4 kJ mol^{-1} (dark blue) and of 25.8 kJ mol^{-1} (light blue) are shown for comparison; at these lower collision energies, only singlet dicarbon reacts.

extended to higher energies based on the additional kinetic energy of the dicarbon reactant as compared to the experiments conducted at collision energies of 22.4 kJ mol^{-1} and of 25.8 kJ mol^{-1} . The corresponding center-of-mass angular distribution is also more forward-scattered thus adding to the conclusion derived from lower collision energies that an osculating cyanoacetylenes complex is involved. On the triplet surface, on the other hand, the center-of-mass translational energy distribution peaks well away from zero translational energy, thus indicating the involvement of a tight exit transition state. The pronounced backward scattered center-of-mass angular distribution presents a distinct and unique feature on the triplet surface and is in strong contrast to the osculation complex patterns as found on the singlet manifold.

What reaction mechanism can be proposed on the triplet surface to account for these findings? A comparison of the experimental data with the triplet potential energy surface (Fig. 17) can shed some light on this issue. Here, the computations identified nine reaction intermediates **t1** to **t9**. Intermediate **t8** can be likely ruled out as the decomposing complex since a fragmentation of the latter has no exit barrier; therefore, we would expect a close to zero peaking of the center-of-mass

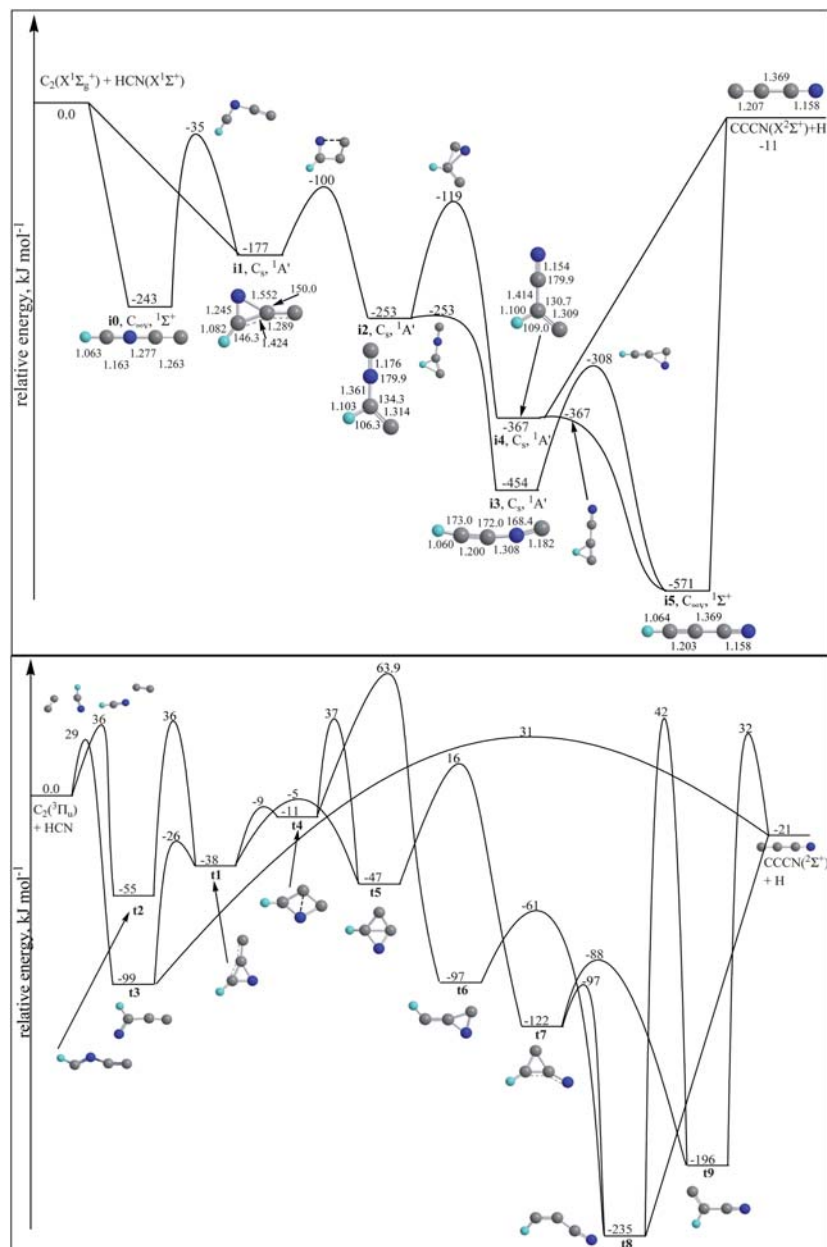


Fig. 17 Schematic triplet potential energy surface of the reaction of triplet dicarbon with hydrogen cyanide. The singlet surface is taken from ref. 29 and shown for comparison.

translational energy distribution. This was clearly not observed on the triplet surface. An alternative reaction pathway of **t8** is the isomerization to **t9** via a barrier located 42 kJ mol⁻¹ above the separated products. Since the energetically more favorable pathway of a decomposition of **t8** to CCCN plus atomic hydrogen was not observed, we can conclude that a [1,3]-hydrogen shift in **t8** to **t9** is unlikely to proceed. Therefore, we can conclude that **t8** does not play a significant role in the scattering dynamics. This holds an important conclusion. According to the calculations, **t8** can be only formed from **t7** via a barrier located 98 kJ mol⁻¹ below the separated reactants; a competing pathway of **t7** presents the isomerization to **t8**. Since this barrier is even higher than the calculated barrier of the non-observed rearrangement of **t7** to **t8**, we may conclude that **t9** cannot be accessed from **t7** either. Therefore, **t7** together with **t8** and **t9** are likely unimportant reaction intermediates on the triplet surface. Is this a reasonable conclusion? It is important to stress that **t7** can be formed only from isomerization of **t5**; the isomerization of **t6** to **t4** can be excluded since the barrier involved ranges at 64 kJ mol⁻¹ with respect to the separated reactants; this is higher than our collision energy of 42.4 kJ mol⁻¹. Intermediate **t5** on the other hand is accessible via **t1** and through a two step sequence involving **t1** and **t4**. On the other hand, considering the locations of the barriers involved, **t1** isomerizes preferentially to **t3**. Therefore, we can conclude that the formation of **t5** is hindered due to the facile isomerization of **t1** to **t3**. Based on these arguments, we limited our discussion to intermediates **t1** to **t3**. The calculations identified two entrance channels, *i.e.* an addition of triplet dicarbon to the carbon and nitrogen atom of the hydrogen cyanide molecule leading to intermediates **t3** and **t2**. Both pathways have entrance barriers of about 29 and 36 kJ mol⁻¹. Recall that in previous experiments at lower collision energies of 22.4 kJ mol⁻¹ and of 25.8 kJ mol⁻¹, these entrance channels were closed. Intermediate **t2** either decomposes back to the reactants or isomerizes to **t1**. Considering the location of the barriers, **t1** in turn isomerizes to intermediate **t3**. The latter can decompose to the observed CCCN isomer in an exoergic reaction (-21 kJ mol⁻¹) via a tight exit transition state located about 50 kJ mol⁻¹ above the separated products. A tight exit transition state was predicted based on the off-peaking of the center-of-mass translational energy distribution of the triplet dicarbon channel (Fig. 16). Therefore, we propose that triplet dicarbon adds preferentially to the carbon atom of the hydrogen cyanide molecule forming intermediate **t3**; this pathway favors the lowest entrance barrier. The latter is relatively short lived; this intermediate can fragment by emitting the heavy CCCN molecule in the backward direction with respect to the triplet dicarbon beam, while the hydrogen atom leaves in the forward hemisphere. These findings amplify the difference in reaction dynamics of singlet *versus* triplet dicarbon with triplet dicarbon.

Having verified the distinct reactivities of singlet and triplet dicarbon with hydrogen cyanide, it is interesting to compare these findings with the isoelectronic dicarbon-acetylene system investigated earlier in our group.³¹ Recall that the reaction of singlet and triplet dicarbon with acetylene was conducted at collision energies between 10.6 and 47.5 kJ mol⁻¹. Here, a singlet dicarbon was found to add without barrier to the acetylene molecule forming intermediate **s1** and/or **s2** (Fig. 22). These collision complexes isomerized yielding ultimately the linear diacetylene molecule (**s3**) which decomposed without exit barrier to the linear 1,3-butadiynyl radical plus atomic hydrogen.¹⁰⁹ Since the diacetylene molecule belongs to the $D_{\infty h}$ point group, the hydrogen atom could be emitted with equal probability from either carbon atom of the rotationally excited diacetylene molecule. Since diacetylene can only be excited to B-like rotations, this results in a forward-backward symmetric center-of-mass angular distribution at all collision energies. On the triplet surface, the rising collision energy resulted in a more pronounced backward scattering of the 1,3-butadiene product. However, the corresponding TOF spectra and laboratory angular distributions could be fit with a single reaction channel. Since the LIF studies provided explicit evidence on the presence of triplet dicarbon, we have re-analyzed the laboratory data for this system with a two-channel fit – one for the

singlet and a second one for the triplet surface. On the singlet surface, we further imposed a forward-backward symmetric center-of-mass angular distribution due to the 'symmetric' diacetylene intermediate. The results are compiled in Fig. 18–21. Indeed, the two channel approach also leads to fits of an identical quality as the single channel approach. Further, on the singlet surface, the translational energy angular distributions all peaked at zero translational energy as expected for a barrierless decomposition of the diacetylene molecule. These are identical patterns as observed for the singlet dicarbon-hydrogen cyanide system. On the other hand, the center-of-mass functions for the triplet channel are quite distinct. First, the

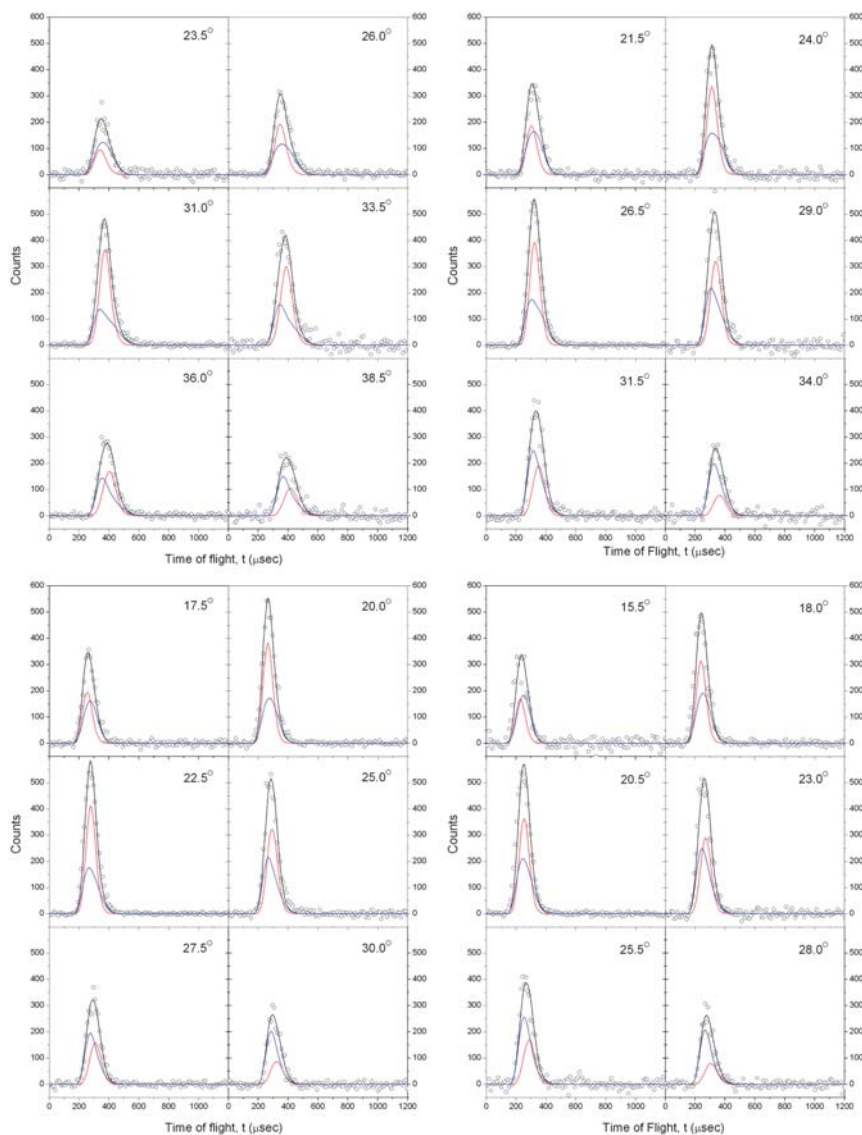


Fig. 18 Time-of-flight spectra recorded at mass-to-charge, m/z , of $m/z = 49$ (C_4H^+) utilizing a two channel fit of the reaction of acetylene with dicarbon leading to the 1,3-butadiynyl radical plus atomic hydrogen at four collision energies of 21.6 (upper left), 29.0 (upper right), 39.9 (lower left), and 47.5 kJ mol^{-1} (lower right). Red: singlet channel; blue: triplet channel.

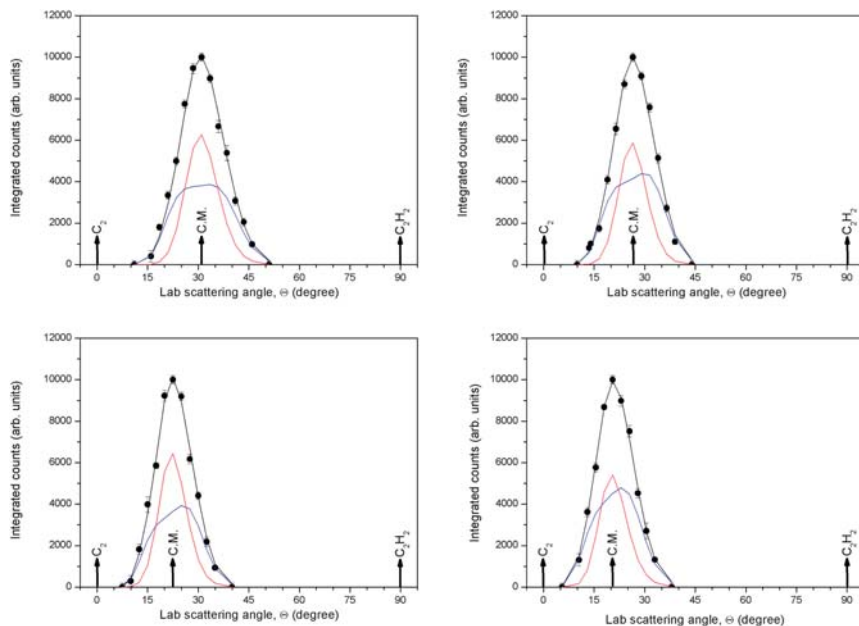


Fig. 19 Laboratory angular distributions at mass-to-charge, m/z , of $m/z = 49$ (C_4H^+) utilizing a two channel fit of the reaction of acetylene with dicarbon leading to the 1,3-butadiynyl radical plus atomic hydrogen at four collision energies of 21.6 (upper left), 29.0 (upper right), 39.9 (lower left), and 47.5 kJ mol^{-1} (lower right). Red: singlet channel; blue: triplet channel.

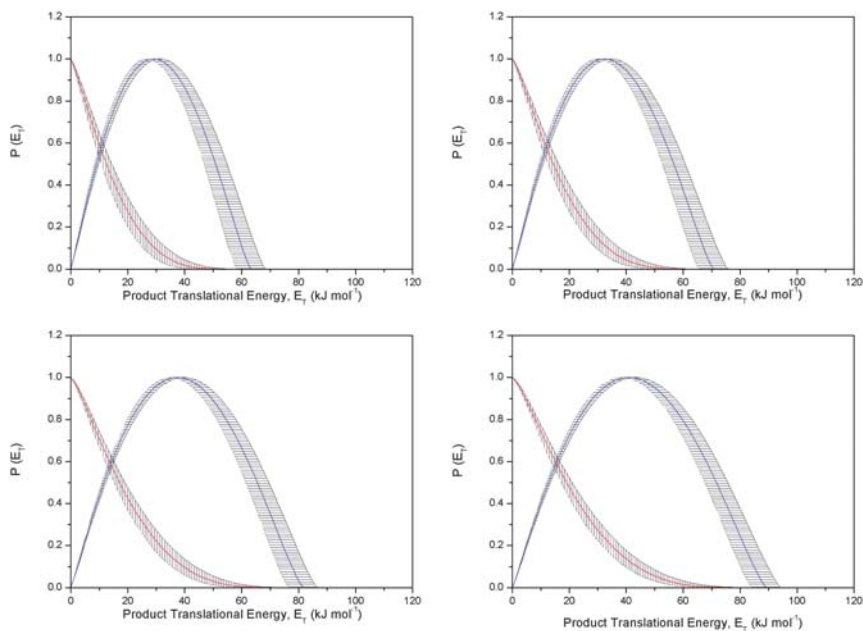


Fig. 20 Center-of-mass translational energy distributions utilizing a two channel fit of the reaction of acetylene with dicarbon leading to the 1,3-butadiynyl radical plus atomic hydrogen at four collision energies of 21.6 (upper left), 29.0 (upper right), 39.9 (lower left), and 47.5 kJ mol^{-1} (lower right). Red: singlet channel; blue: triplet channel.

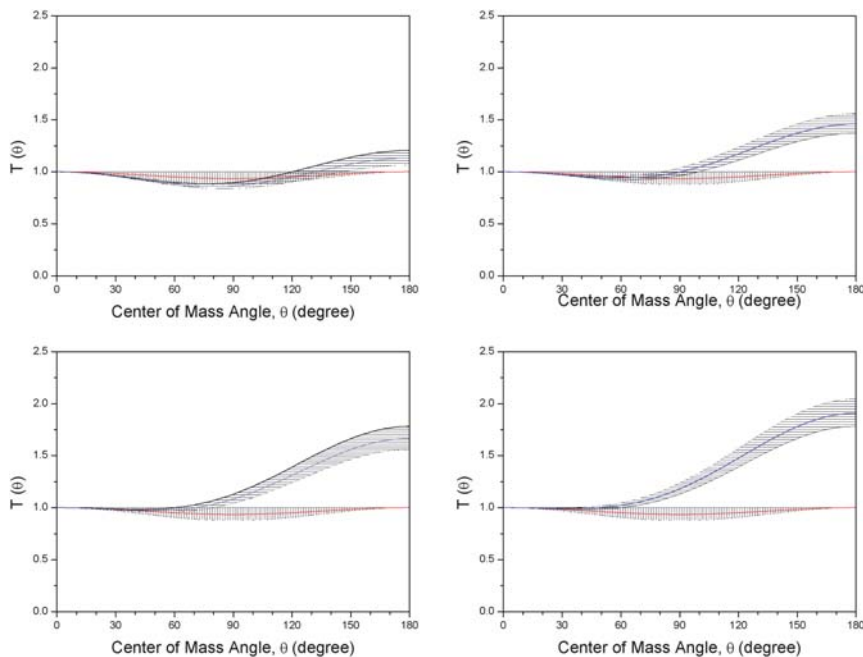


Fig. 21 Center-of-mass angular distributions utilizing a two channel fit of the reaction of acetylene with dicarbon leading to the 1,3-butadiynyl radical plus atomic hydrogen at four collision energies of 21.6 (upper left), 29.0 (upper right), 39.9 (lower left), and 47.5 kJ mol^{-1} (lower right). Red: singlet channel; blue: triplet channel.

translational energy distributions (Fig. 20) depict well-pronounced maxima as characteristic for a tight exit transition state. The existence of a tight exit transition state is verified by the triplet potential energy surface; here, intermediate **t3** decomposes to 1,3-butadienyl radicals plus atomic hydrogen (Fig. 22); **t3** is formed initially *via* isomerization of the initial collision complexes **t1** and **t2**. Secondly, the center-of-mass angular distributions are increasingly backward scattered as the collision energy rises (for all systems investigated here, we have almost constant triplet to singlet dicarbon ratios of about three to one). Therefore, this trend cannot be explained with an increase in the concentration of triplet dicarbon in the beam. However, as extracted from the LIF studies, as the collision energy rises from 21.6 to 47.5 kJ mol^{-1} , so does the rotational temperature increase from about 100 K to about 350 K. Therefore, these results suggest that the increased rotational temperature of the triplet dicarbon beam and the enhanced collision energy might be responsible for an enhancement in the backward-scattering. Recall that the reaction channel of triplet dicarbon with isoelectronic hydrogen cyanide also leads to a backward-scattered center-of-mass angular distribution (Fig. 16). There seems to be – at least in the case of acetylene and hydrogen cyanide – some consistency that the enhanced rotational temperature of dicarbon and/or the rising collision energy leads to an amplification of the scattering signal in the backward hemisphere.

Finally, we would like to comment briefly on preliminary results of the reaction of methylidyne radicals with diacetylene (C_4H_2) and methylacetylene (C_3H_4) (Fig. 23). Here, preliminary data suggest that in both systems, the methylidyne radical formally replaces at least a hydrogen atom leading to the products of the generic formulae C_3H_2 and C_4H_4 , respectively. Those preliminary data demonstrate the feasibility of the reactions of methylidyne radicals with hydrocarbons of relevance

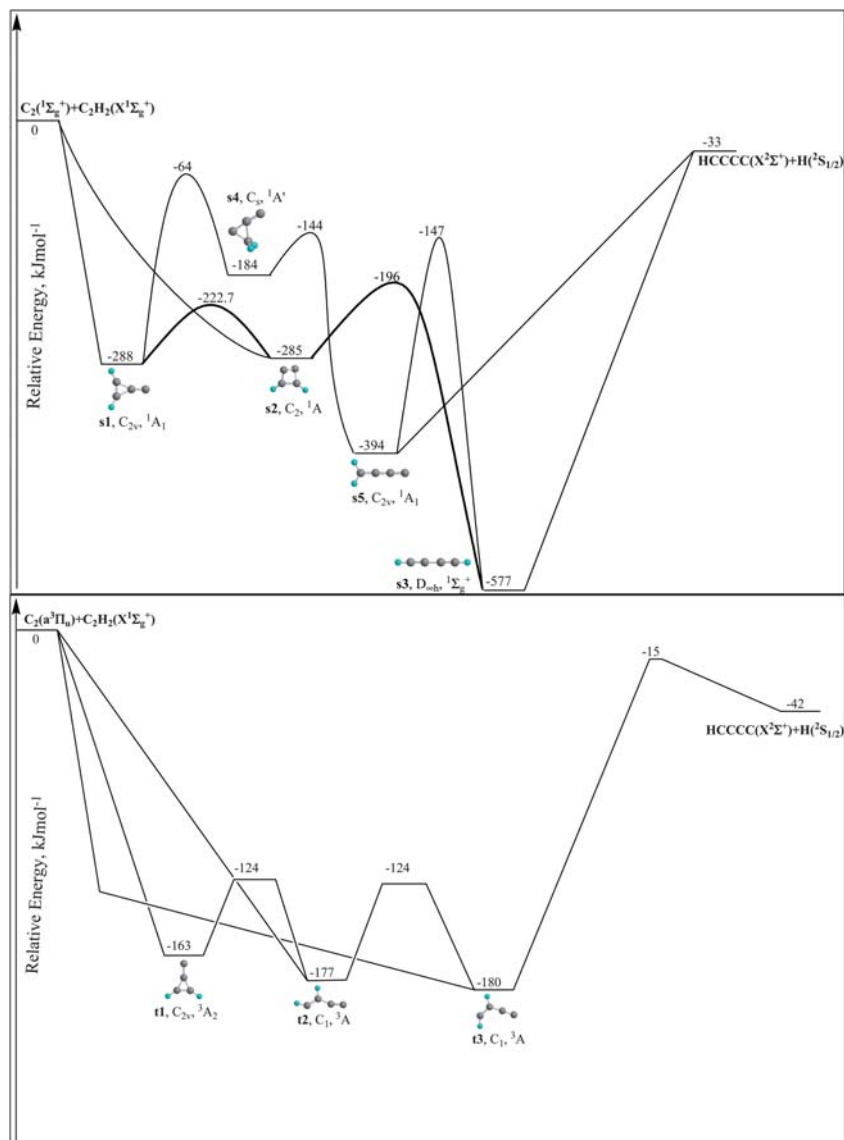


Fig. 22 Potential energy surfaces (PES) of the reactions of C₂(X¹Σ_g⁺) (upper) and C₂(a³Π_u) (lower) with acetylene, C₂H₂(X¹Σ_g⁺), adapted from ref. 31.

to Titan's atmosphere and depict the capability to conduct scattering experiments under single collision condition with this important diatomic radical species.

4.2. Surface scattering experiments

4.2.1. Ethane ices. Fig. 24(a) displays the mid-infrared spectrum of pristine ethane (C₂H₆) ice at 50 K. In the higher frequency region of the spectrum, the fundamental bands associated with the ν₁₀ (2970 cm⁻¹) and the ν₅ (2878 cm⁻¹) CH₃ stretching vibration modes are clearly visible as the strongest absorption features. The deformation modes associated with the methyl (CH₃) group are located at lower frequencies, specifically the ν₁₁ CH₃ deformation region (1468–1450 cm⁻¹), the ν₆

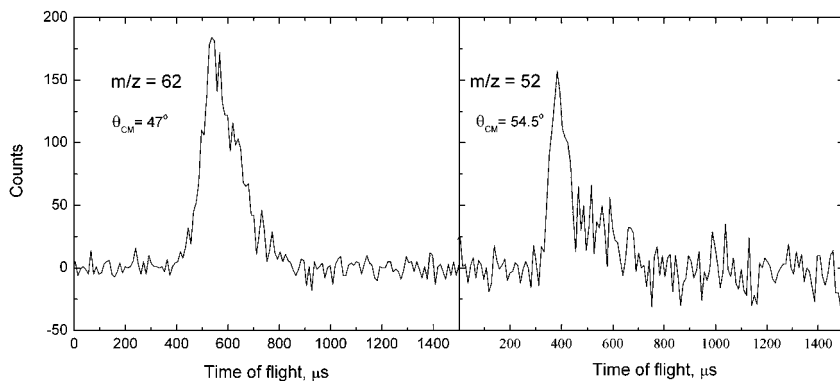


Fig. 23 Time-of-flight spectra of the C_5H_2 and C_4H_4 reaction products as detected *via* their molecular ions at $m/z = 62$ and 52 in the reaction of the methylidyne radical with diacetylene (left) and methylacetylene (right) at the corresponding center-of-mass angles.

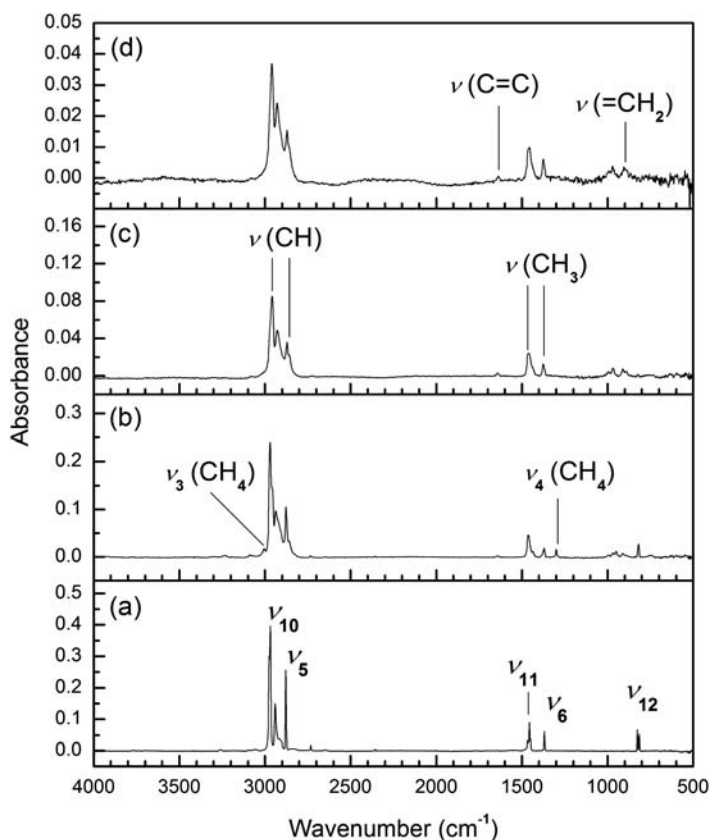


Fig. 24 Mid-infrared spectra of (a) pristine ethane ice at 50 K, (b) electron irradiated (500 nA, 3 h) ethane ice at 50 K, (c) electron irradiated ethane ice heated to 94 K, and (d) electron irradiated ethane ice heated to 300 K. Band assignments are compiled in Tables 1 and 2.

Table 1 Vibrational assignments of pristine ethane ice (C₂H₆) at 50 K

Pristine absorption/cm ⁻¹	Literature value ^a /cm ⁻¹	Assignment
2970	2972	ν_{10} (CH ₃ stretch)
2941	2941	$\nu_8 + \nu_{11}$ (combination)
2878	2879	ν_5 (CH ₃ stretch)
2733	2736	$\nu_2 + \nu_6$ (combination)
1468–1450	1464	ν_{11} (CH ₃ deform)
1369	1370	ν_6 (CH ₃ deform)
825–815	820	ν_{12} (CH ₃ rock)

^a Kim *et al.*¹¹²

CH₃ deformation band positioned at 1369 cm⁻¹, and the ν_6 CH₃ rocking doublet located at the 825 and 815 cm⁻¹ positions. All peaks, which are summarized in Table 1, are in good agreement with literature values assigned to crystalline phase ethane ices.¹¹⁰

Having discussed the assignments in the pristine ethane sample, Fig. 24(b) depicts the mid-infrared spectrum of the sample after the 3 h exposure to 5 keV electron irradiation at a nominal current of 500 nA. The absorption features observed in the irradiated ethane sample are compiled in Table 2. Most absorption bands previously assigned to the CH stretching modes of the ethane molecule are observed to decrease in intensity and become broader in appearance. In the lower frequency region, a similar result is observed for the CH₃ deformation modes, where the ν_6 CH₃ rocking doublet originally located at 825 and 815 cm⁻¹ for the neat C₂H₆ ice sample combines into the one broad peak located at 820 cm⁻¹ in the irradiated sample spectrum. This indicates that the crystalline ethane ice converts to an amorphous phase over the irradiation process.¹¹¹ A number of new absorption features, not previously identified in the pristine ethane sample are also observed in the lower frequency region of Fig. 24(b) at 1642, 1435, 1299, 993, 969, 949 and 911 cm⁻¹; these vibrations

Table 2 Proposed vibrational assignments for residue formed from irradiated ethane ice (C₂H₆)

50 K/cm ⁻¹	94 K/cm ⁻¹	300 K/cm ⁻¹	Assignment ^a	Literature ^a /cm ⁻¹
3006	—	—	ν_3 (CH ₄) ^b	3008 ^b
2971	2958	2960	(Asym. CH ₃ stretch)	2975–2950
2938	2929	2930	(Asym. CH ₂ stretch)	2940–2915
2878	2871	2871	(Sym. CH ₃ stretch)	2885–2865
2736	2724	—	Combination	—
1642	1642	1640	(C=C stretch)	1665–1630
1463	1462	1458	(CH ₃ deform)	1465–1440
1435	—	—	—	—
1371	1374	1375	(CH ₃ deform)	1390–1370
1299	—	—	ν_4 (CH ₄) ^b	1300 ^b
993	993	—	(HC=CH wag)	1000–910
969	969	970	(CH ₃ rock)	1060–900
949	—	—	—	—
911	911	911	(=CH ₂ wag)	980–810
—	891	—	—	—
820	820	—	(CH ₂ rock)	800–700

^a Tejada *et al.*¹¹⁰ ^b Kim *et al.*¹¹²

are assigned predominantly to saturated carriers and to a minor amount to olefinic functional groups. We then warmed up the sample at a rate of 0.5 K min^{-1} . Fig. 24(c) displays the mid-infrared spectrum of the irradiated ethane sample heated to 94 K with the observed absorption features compiled in Table 2. With the sublimation of ethane occurring in the 60–70 K temperature range, it is expected that absorption features associated with the original ethane sample would no longer be observed at 94 K. However, absorption features located in the high frequency region of the C–H stretching fundamentals are still clearly visible, displaying intensities $\sim 20\%$ of the original ethane bands. These absorption bands are all shifted to the red in the order of $\sim 10 \text{ cm}^{-1}$ from the original positions of the corresponding ethane peaks. This suggests that although the neat ethane sample sublimates at 60–70 K, the irradiated sample and the newly formed molecules can still retain ethane at elevated temperatures higher than the nominal sublimation temperature. In addition, the CH_3 deformation bands are also still present at 94 K at 1462 cm^{-1} and 1374 cm^{-1} ; they do not display a significant shift from the positions assigned in non-irradiated ethane at 50 K. The irradiation induced 1435, 1299 and 949 cm^{-1} bands, previously identified in the 50 K irradiation spectrum, were observed to disappear after heating to 94 K. Finally, Fig. 24(d) displays the mid-infrared spectrum of remaining residues that were formed from the electron irradiation of ethane after heating the substrate to 300 K. The spectrum is similar in appearance to the spectrum recorded at 94 K in relation to peaks and their positions, except for the observation that the absorption intensities for all bands appear to be approximately 50% of those recorded at 94 K. These absorptions are indicative of a polymeric residue, containing mostly saturated, aliphatic groups and only to a minor amount olefinic units.

In an effort to correlate the observation of new absorption bands to species formed *via* electron irradiation of ethane ices, a mass spectroscopic analysis of the gas phase was performed during controlled heating of the sample from 50 K to 300 K. Fig. 25 displays the ion count profiles of methane (CH_4) and ethane (C_2H_6) generated during the warm-up phase of the pristine ethane ice (Fig. 25(a)) and after the electron irradiation (Fig. 25(b)). No new species were detected in the mass spectra of the gas phase during the actual irradiation period, but only during the sublimation phase of the irradiated ices. Signals for $m/z = 30$ (C_2H_6^+) developed in the range of 60 K to 70 K for the heated pristine sample, confirming the sublimation temperature for neat ethane under the present experimental conditions. However, after exposure to electron irradiation, the signal for the C_2H_6^+ species ($m/z = 30$) also started to increase at 60 K before reaching a 2×10^{-9} ion count maxima at 70 K. However, the signal for C_2H_6^+ in the irradiation experiment differed from the neat sample by the observation of an extended sublimation

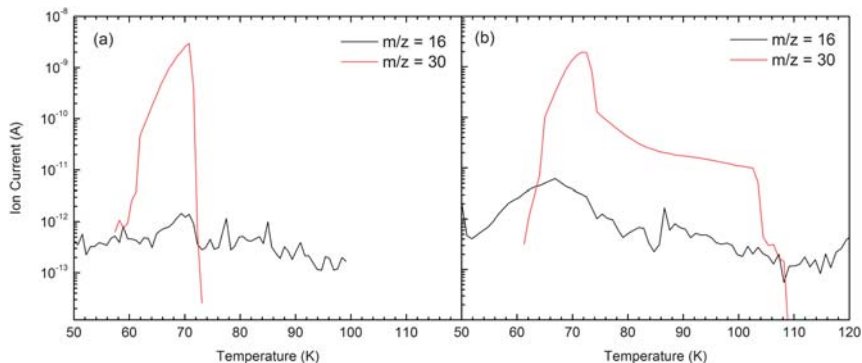


Fig. 25 Ion-count profiles of methane (CH_4) and ethane (C_2H_6) released during the warm-up phase after (a) 0 nA (b) 500 nA irradiation of ethane at 50 K.

temperature profile where ethane was only observed to stop out-gassing at 105 K. In addition, the signal for $m/z = 16$ (CH_4^+) increased between in the 52 K to 80 K temperature range after heating of the irradiated sample. This sublimation temperature range corresponds well with the sublimation profile of CH_4 previously confirmed by Kim *et al.*¹²² using similar experimental conditions, allowing for the positive identification of methane as a degradation product of the irradiated ethane ices in the present study. However, it is important to note that ethane itself contributes to $m/z = 16$ due to electron impact ionization as shown in Fig. 24(a), meaning the blank contribution in the pristine ices must be subtracted to quantifying the methane signal in the irradiation experiments. It should be stressed that no higher molecular weight alkanes were observed to sublime in the irradiated sample.

The electron irradiation of the ethane ice at 50 K resulted in the observation of methane as a primary deposition product. This species is identified in the solid phase by the 3004 cm^{-1} ν_3 (CH_4) stretching fundamental band and the 1299 cm^{-1} ν_4 (CH_4) deformation fundamental band in the associated mid-IR spectrum (Fig. 24(b)). Further evidence of methane formation is provided by the mass spectrum recorded during the controlled heating of the irradiated ethane film. Here, the ion count profile for $m/z = 16$ (CH_4^+) increased between 50 K and 75 K. The complete sublimation of methane after heating the cold target to 94 K is confirmed by the mid-infrared spectrum recorded in Fig. 24(c), where the absorption bands previously attributed to the methane fundamentals disappeared.

As the mass spectrum recorded for the irradiated ethane sample confirms the total sublimation of the original ethane ice at 105 K, we can now shift our attention to the residue remaining on the silver substrate after heating to 300 K. The infrared spectrum presented in Fig. 24(d) clearly displays absorption features that can be attributed to a solid phase hydrocarbon formed as a product of the irradiation. High-frequency absorption bands in the $3000\text{--}2850\text{ cm}^{-1}$ region are clearly visible, which are typical of C–H stretching vibrations in aliphatic hydrocarbons. The observation of a distinct absorption band located at 2938 cm^{-1} , a region generally associated with the asymmetric stretching mode of C–H in alkane $-\text{CH}_2-$ chain groups ($2940\text{--}2915\text{ cm}^{-1}$), suggests that ethane ices form extended aliphatic hydrocarbons upon irradiation.

Recent experiments conducted by Kim *et al.*¹¹² using 10 and 100 nA electron beam currents and lower irradiation time of only 60 min have confirmed the irradiation induced formation of n-butane. Although absorption bands could be tentatively assigned to the fundamental modes of the n-butane species in the present study, the absence of a ion count signal at $m/z = 58$ ($\text{C}_4\text{H}_{10}^+$) over its 90 K to 100 K sublimation

Table 3 Vibrational assignments of pristine propane ice (C_3H_8) at 65 K

Pristine absorption/ cm^{-1}	Literature value ^a / cm^{-1}	Assignment
2964	2962	ν_2 (CH_3 stretch)
2935	—	ν_{23} (CH_2 stretch)
2893	2887	ν_{16} (CH_3 stretch)
2871	2887	ν_3 (CH_2 stretch)
2731	2752	$\nu_2 + \nu_6$ (combination)
1472 – 1461	1475–1460	$\nu_4, \nu_5, \nu_{17}, \nu_{24}$ (CH_3 deform)
1389 – 1368	1382–1368	ν_6, ν_{18} (CH_3 deform)
1186	1185	ν_{25} (CH_2 rock)
1155	1155	ν_7 (CH_2 rock)
1049	1050	ν_{20} (CC stretch)
868	869	ν_8 (CC stretch)
747	745	ν_{26} (CH_2 rock)

^a Goodman *et al.*¹¹³

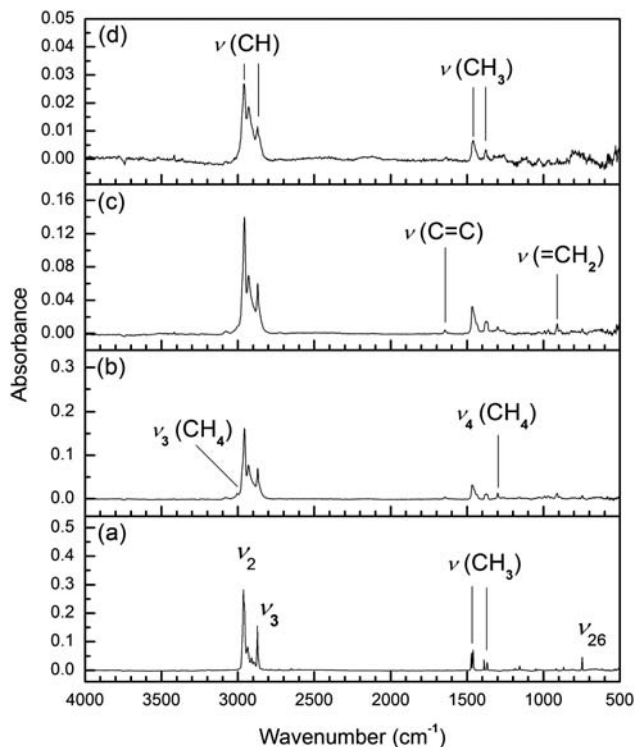


Fig. 26 Mid-infrared spectra of (a) pristine propane ice at 65 K, (b) electron irradiated (500 nA, 3 h) propane ice at 65 K, (c) electron irradiated propane ice heated to 94 K, and (d) electron irradiated propane ice heated to 300 K. Band assignments are compiled in Tables 3 and 4.

range in the corresponding mass spectra indicates that n-butane was not formed under the present irradiation conditions. After consideration of the absorbed energy dosages per ethane molecule, where the previous study calculated a total dosage of 1.4 ± 0.2 eV molecule⁻¹ compared to 36 ± 2 eV per molecule calculated for the present experiments, it could be expected that the much higher irradiation dose would induce a continued 'polymerization' of any n-butane formed into higher order aliphatic alkanes.

It is observed through the absorption intensities assigned to the 2960 cm^{-1} asymmetric CH₃ stretching vibration and the 2960 cm^{-1} asymmetric CH₂ mode of the residue, that the methyl functional group is the stronger of the two absorbing modes. This indicates that the product residue may display a considerable amount of branching in its structure, as opposed to linear aliphatic conformations which would display a greater absorption intensity for the $-\text{CH}_2-$ chain species. In addition, the 300 K mid-infrared spectrum of the residue provides evidence for unsaturated vinylenes centers at 1640 cm^{-1} (C=C stretch) and terminal vinyl groups ($=\text{CH}_2$) at 911 cm^{-1} . This indicates also hydrogen loss under the irradiation conditions.

4.2.2. Propane ices. Fig. 26(a) displays the mid-infrared spectrum for pristine propane ice at 65 K. The associated peak positions and assignments are summarized in Table 3. In the C–H stretching region of the spectrum, the absorption bands associated with the terminal ν_2 (2964 cm^{-1}) and ν_{16} (2893 cm^{-1}) CH₃ stretching modes can be identified. This is in addition to the main chain ν_{23} (2935 cm^{-1}) and ν_3 (2871 cm^{-1}) CH₂ stretching fundamental vibrations that are also observed as strong absorption peaks. The CH₃ deformation vibrations are identified in their

characteristic positions for aliphatic hydrocarbons, specifically in the regions located at (1472–1461 cm^{-1}) and (1389–1368 cm^{-1}) where a number of CH_3 deformation vibrations share similar vibrational frequencies (Table 3). The final low frequency absorption bands identified in the spectrum of pristine C_3H_8 ice can be assigned to the ν_{20} and ν_8 C–C stretching vibrations located at 1049 and 868 cm^{-1} respectively and the ν_{25} , ν_7 and ν_{26} CH_3 rocking vibrations in their respective 1186, 1155 and 747 cm^{-1} positions. All absorption bands observed in the current experimental spectra appear to correspond well with published values previously assigned to the crystalline ethane at 77 K.¹¹³

Fig. 26(b) depicts the mid-infrared spectrum of the sample after 3 h exposure to 5 keV electron irradiation at 500 nA at 65 K. Absorption bands and associated peak assignments for the irradiated propane ice spectrum are compiled in Table 4. There appears to be significant alteration to the original C_3H_8 band positions for the C–H stretching modes after irradiation, with most peaks experiencing a 4–6 cm^{-1} shift to lower frequency. This is in addition to displaying an approximate 40% decrease in absorption intensity and a noticeable peak broadening effect. A clear loss in fine structure is also displayed for the CH_3 deformation bands following irradiation, where the previously well-defined peaks in the 1472–1461 cm^{-1} and 1389–1368 cm^{-1} regions appear to combine into two separate diffuse features. In addition, novel absorption features that were not previously identified in the non-irradiated C_3H_8 ice spectrum, are also observed across the entire mid-infrared region of Fig. 26(b). These weak features can be observed at 3075, 3004, 1645, 1299, 993, 970 and 910 cm^{-1} . Again, these can be mainly attributed to hydrogen-rich aliphatic molecules.

Fig. 26(c) displays the mid-infrared spectrum of the irradiated propane sample at 94 K. The observed absorption features are compiled in Table 4. Sublimation of propane was observed to occur in the 70 K to 90 K temperature range from the controlled heating of the pristine propane ice sample; therefore it is expected that very little of the original propane sample would be left on the silver substrate to contribute to the absorption spectrum at 94 K. However, it can be observed in Fig. 26(c) that, similar to the delayed emission of the ethane ice, the high frequency C–H stretching bands are still clearly visible with only slightly lower absorption intensities than those recorded at 65 K after irradiation. Furthermore, the new

Table 4 Possible vibrational assignments for residue formed from irradiated propane ice (C_3H_8)

65 K/ cm^{-1}	94 K/ cm^{-1}	300 K/ cm^{-1}	Assignment ^a	Literature ^a / cm^{-1}
3075	3072	3075	(= CH_2 stretch)	3150–3000
3004	—	—	ν_3 (CH_4) ^b	3008 ^b
2957	2957	2959	(Asym. CH_3 stretch)	2975–2950
2930	2929	2930	(Asym. CH_2 stretch)	2940–2915
2870	2869	2871	(Sym. CH_3 stretch)	2885–2865
1645	1645	1635	(C=C stretch)	1665–1630
1467	1466	1460	(CH_3 deform)	1465–1440
1375	1373	1375	(CH_3 deform)	1390–1370
1299	1299	—	ν_4 (CH_4) ^b	1300 ^b
993	991	—	(HC=CH wag)	1000–910
970	968	967	(CH_3 rock)	1060–900
910	910	910	(= CH_2 wag)	980–810
748	747	—	ν_{26} (C_2H_6)	745 ^c

^a Goodman *et al.*¹¹³ ^b Kim *et al.*¹¹²

absorption peaks that were identified in the irradiated ice spectrum at 65 K could all be accounted for at 94 K.

Finally, Fig. 26(d) displays the mid-infrared spectrum of the irradiated propane ice after heating to 300 K. At 300 K any original propane should have long been sublimated from the cold target, leaving only a residue on the substrate. It is clear from the spectrum at 300 K that a residue is formed from the irradiation of the propane ice, with weakly absorbing C–H peaks clearly identified above the baseline in the 2960–2870 cm^{-1} region. Furthermore, absorption features corresponding to the CH_3 deformation modes at 1460 and 1375 cm^{-1} can be identified in the lower frequency regions, as well as the 1635, 967 and 910 cm^{-1} bands that remain after first being identified as irradiation induced features at 65 K.

Mass spectroscopy was employed for the gas phase analysis of sublimated propane during the controlled heating of the sample from 50 K to 300 K. Fig. 27(a) displays the ion count profiles of propane generated during the warm-up phase of the pristine propane ice, while Fig. 27(b) displays the ion count profile of propane during the controlled heating of the sample following electron irradiation. Surprisingly, no newly formed alkanes were observed in the mass spectra collected, neither during the actual irradiation period nor during the warm-up phase of the irradiated propane ices. Signals for $m/z = 44$ (C_3H_8^+) generated by the heated pristine sample were observed to increase in the range of 70–90 K (2×10^{-9} maximum ion count), correlating to the sublimation temperature for propane under the present experimental conditions. Following the irradiation of the propane sample, the ion current for the C_3H_8^+ species reached a maximum ion count of 5×10^{-10} at 86 K. The sublimation profile of the irradiated propane sample was observed to extend to 94 K, the only discernable difference between the shape of the pristine and irradiated propane ice gas phase sublimation profiles.

The mid-infrared spectrum obtained for irradiated propane ices after controlled heating to 300 K depicts the remaining hydrocarbon residue after sublimation of volatile species from the substrate surface. The general appearance of the residue spectrum is similar to the spectrum of the residue obtained from the irradiated ethane ices discussed earlier. Although the peaks observed in the propane spectrum are about 25% lower in absorption intensity than those observed in the irradiated ethane experiment, the basic patterns are generally the same. The distinctive C–H stretching modes identified at 2959 (asymmetric CH_3), 2930 (asymmetric CH_2) and 2871 cm^{-1} (symmetric CH_3); in addition to the positive identification of CH_3 group deformation modes at 1460 and 1375 cm^{-1} , all indicate that the residue consists of large hydrocarbon molecules with sublimation temperatures above 300 K. It can therefore be concluded that the irradiated propane molecules, each

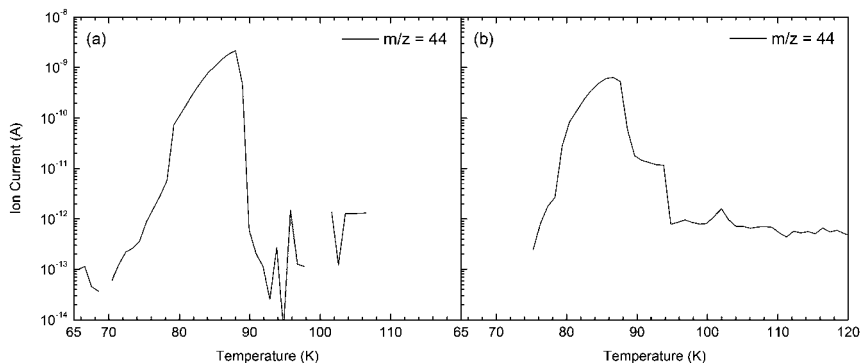


Fig. 27 Ion-count profiles of propane (C_3H_8) released during warm-up phase after (a) 0 nA (b) 500 nA irradiation of propane at 65 K.

exposed to 53 ± 5 eV per molecule, undergo extensive polymerization to form higher-order aliphatic hydrocarbons. In an effort to quantify the conversion of propane to the polymer, an integration of the $m/z = 44$ ($C_3H_8^+$) signals for both the 0 nA and 500 nA mass spectra was performed. A comparison of the signal of propane of the irradiation experiment (3.7×10^{-7} As) to the blank experiment (1.1×10^{-6} As) suggests that about 66% of the propane molecules underwent an irradiation induced alteration; this translates to a loss of $7.2 \pm 0.2 \times 10^{16}$ propane molecules. In our experiments, we irradiated the sample with 1.5×10^{16} electrons per cm^2 . Since each electron deposits 410 ± 10 eV into the sample, this leads to a total energy deposition of 6.2×10^{18} eV cm^{-2} . Recall that Titan's energy deposition is of 4.5×10^9 eV $cm^{-2} s^{-1}$ on its surface. Therefore, the irradiation time in our laboratory corresponds to about 44 years exposure time on Titan. In these 44 'Titan' years, about 5×10^{-6} g of propane are transformed into a polymeric structure per cm^2 . Over a typical time of 10^9 years, this results into an accumulation of about 116 g polymeric material per cm^2 . Considering a typical density of 0.94 g cm^{-3} for a low density organic polymer, this results in a layer of about 1.2 meter polymer per cm^2 . Therefore, our laboratory experiments show that in principle, propane can be converted to aliphatic-type polymers over geological timescales on Titan's surface *via* interaction with cosmic ray particles.

4.3. VUV photoionization studies

Fig. 28 shows a mass spectrum of the products formed from ablation of a silicon rod in a carrier gas of acetylene recorded at a photon energy of 10.5 eV. The inset in Fig. 28 depicts an expanded spectrum between 49–55 amu to demonstrate the resolution and quality of the mass spectrum. The spectrum is complex, but in conjunction with tunable VUV radiation allows for elucidation of the chemical composition *via* ionization energy determinations coupled with calculated results performed in this work and literature values. In Table 5, the most prominent masses are compiled along with their chemical identification. Also presented are calculated and measured ionization energies for a number of these species and previous literature results are

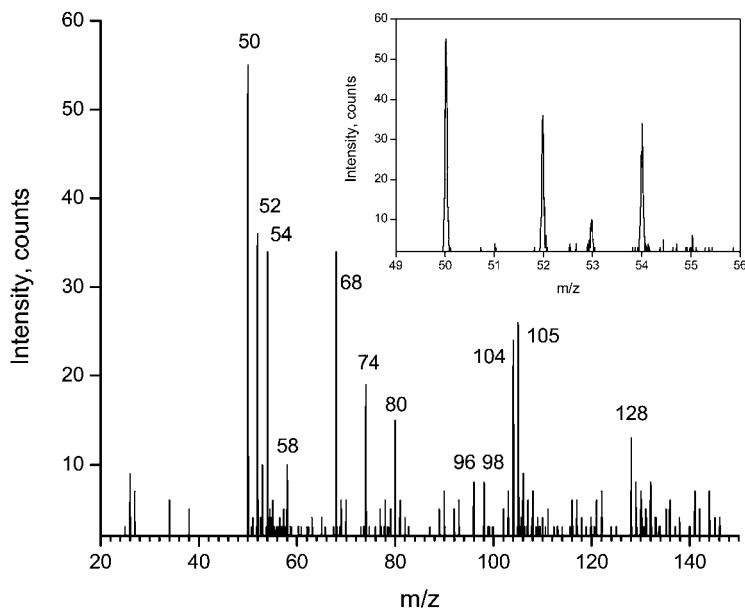


Fig. 28 Mass spectrum at photon energy of 10.5 eV.

Table 5 Mass, chemical species, measured and calculated ionization energies. All energies in eV.^a







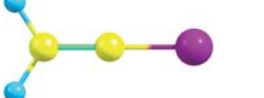
Mass	Species	IE _{exp}	IE _{calc}	Literature IE
52	SiC ₂	9.75(±0.025)		10.2 ± 0.3 ^b , 10.321 ^d , 9.69(l) ^f , 9.79(c) ^f , 10.4 ± 0.3 ^h
53	SiC ₂ H	9.1		7.06 ^e
			7.26 (v) 7.26 (a)	
			8.10 (v) 6.96 (a)	
			9.54 (v) 9.02 (a)	
			9.26 (v)	
54	SiC ₂ H ₂	9.3(±0.05)		8.97(a) ^g , 9.83(v) ^g , 9.00(c) ^e
			9.50 (v) 9.31 (a)	
			9.14 (v) 8.72 (a)	
			8.37 (v) 8.26 (a)	
68	Si ₂ C	9.2(±0.025)		9.2 ± 0.3 ^b , 9.06–9.33 ^c , 9.626 ^d , 9.18(l) ^f , 9.19(c) ^f , 9.5 ± 0.5 ^h
80	Si ₂ C ₂	8.95(±0.05)		7.731 ⁱ , 8.2 ± 0.3 ^b , 8.259 ^d , 8.24 ^j , 8.97(c) ^f , 8.8 ± 0.5 ^h
81	Si ₂ C ₂ H	8.2(±0.1)		
82	Si ₂ C ₂ H ₂	9.4		

Table 5 (Contd.)

Mass	Species	IE _{exp}	IE _{calc}	Literature IE
92	Si ₂ C ₃	8.7(±0.1)		8.12(l) ^f
96	Si ₃ C	8.4(±0.1)		8.2 ± 0.3 ^b , 7.95–8.3 ^c , 8.679 ^d , 7.81(c) ^f , 7.9 ± 0.5 ^h
104	Si ₂ C ₄	8.45(±0.05)		
105	Si ₂ C ₄ H	8.45(±0.05)		
106	Si ₂ C ₄ H ₂	8.5(±0.05)		
108	Si ₃ C ₂	8.5(±0.1)		7.27(c) ^f
116	Si ₂ C ₅	<8.0		
128	Si ₂ C ₆	8.5(±0.1)		
129	Si ₂ C ₆ H	—		
130	Si ₂ C ₆ H ₂	8.5		
136	Si ₄ C ₂	8.5(±0.1)		

^a V – vertical ionization energy, A – adiabatic ionization energy, (l) – linear, (c) – cyclic.

^b Reference, Drowart *et al.*¹¹⁶ ^c Reference, Boldyrev *et al.*¹²¹ ^d Reference, Pradhan *et al.*¹²⁰

^e Reference, Ketvirtis *et al.*¹¹⁵ ^f Reference, Yadav *et al.*¹¹⁹ ^g Reference, Ikuta *et al.*¹¹⁴

^h Reference, Schumde *et al.*¹¹⁷ ⁱ Reference Hou *et al.*¹²⁴ ^j Reference Parent *et al.*¹²²

also reported in this Table. The following species are ionized in the molecular beam at 10.5 eV: polyynes (C₄H₂, C₆H₂, C₈H₂, C₁₀H₂), molecules belonging to the SiC₂H_x family ($x = 0, 1, 2$), to the Si₂C₂H_x family ($x = 0, 1, 2$), silicon–carbon clusters Si₂C_x ($x = 1–6$), Si₃C, Si₃C₂, and Si₄C₂, as well as Si₂C₄H_x ($x = 1, 2$) and Si₂C₆H_x ($x = 1, 2$). A comprehensive investigation of the ionization energies of all these species is beyond the scope of this paper. To demonstrate the feasibility of our approach and to highlight the implications to Titan, we focus on the SiC₂H and SiC₂H₂ systems as case studies. Fig. 29 shows the PIE curves of $m/z = 53$ and 54 corresponding to the ions of SiC₂H and SiC₂H₂.

Considering SiC₂H₂, calculations at the CCSD(T)/cc-pVQZ//B3LYP/6-311G** level suggest that a cyclic structure holding C_{2v} symmetry and in the ¹A₁ electronic ground state is the lowest lying state. A vertical ionization energy (VIE) of 9.5 eV and adiabatic ionization energy (AIE) of 9.3 eV is derived for ionization to a C_{2v} symmetry and ²A₁ state of the cation. The calculated adiabatic ionization energy agrees perfectly with our 9.3 eV experimental determination. An L shaped isomer in which silicon inserts between a carbon and hydrogen of the acetylene lies 78.3 kJ mol⁻¹ above the ground state in the neutral channel with a calculated VIE and AIE of 9.1 and 8.7 eV respectively. There is no signal in our PIE spectrum at these energies and all the other possible isomers lie much higher in energy to be populated in our molecular beam. This suggests that we are exclusively producing the cyclic isomer of SiC₂H₂ in our molecular beam. Ikuta *et al.*¹¹⁴ performed a comprehensive study on the ionization energies for various isomers of SiC₂H₂ at the similar CCSD(T)/cc-pVQZ level of theory. They suggest that the global minima for the neutral and cation, (C_{2v}, ¹A₁) and (C_{2v}, ²B₂) are silacyclopropenyldiene structures with VIE and AIE of 9.83 and 8.97 eV respectively. Ketvirtis *et al.*¹¹⁵ calculated an AIE of 9.00 eV at the QCISD(T)-(full) level of theory. Our measured IE of 9.3 eV is discrepant with these calculations. The difference between our present calculated results and those by Ikuta *et al.*¹¹⁴ can be explained by the discrepancy in the electronic states of the silacyclopropenyldiene cation. Our calculations give the ²A₁ state as the lowest cationic state at the vertical geometry with VIE of 9.50 eV, lower than 9.83 eV obtained by Ikuta *et al.* for the ²B₂ state. Geometry relaxation in the ²B₂ state of the cation is larger than in ²A₁ resulting in the lower AIE for

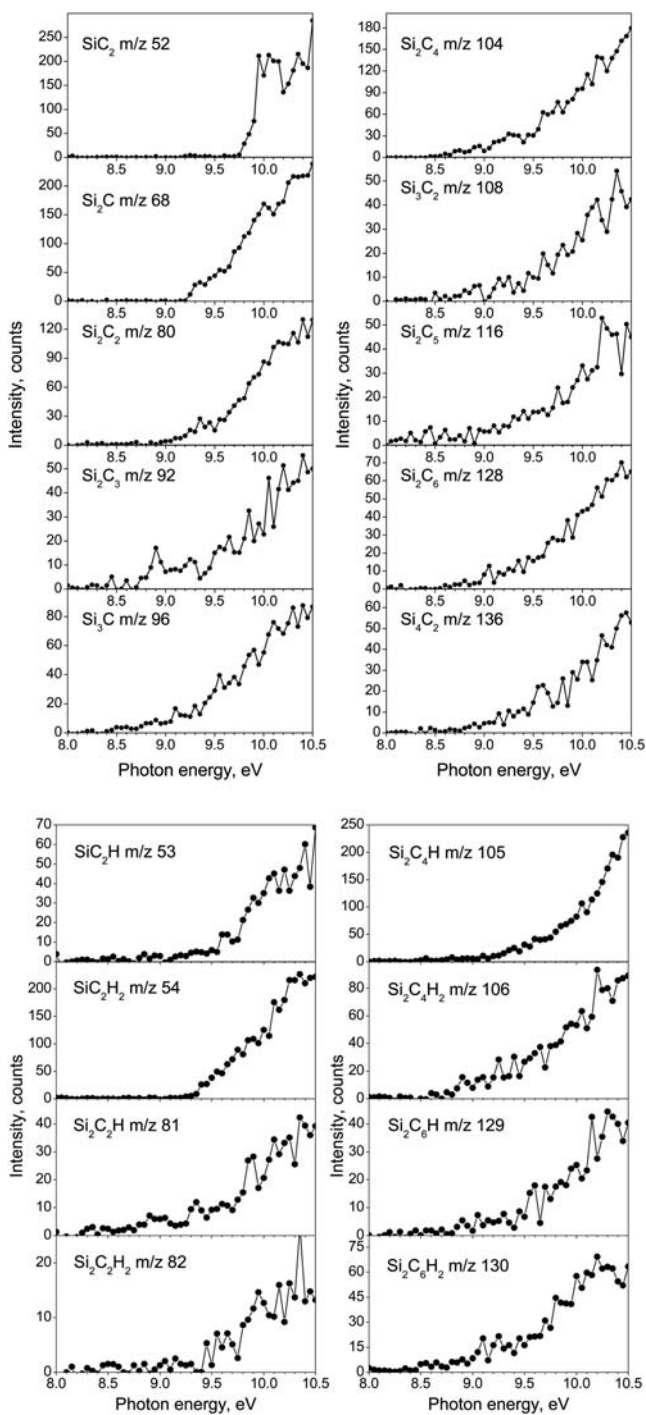


Fig. 29 top: PIE curves for SiC_2 , Si_2C_x , ($x = 1-6$), Si_3C , Si_3C_2 , Si_4C_2 . bottom: PIE curves for SiC_2H , SiC_2H_2 , $\text{Si}_2\text{C}_2\text{H}$, $\text{Si}_2\text{C}_2\text{H}_2$, $\text{Si}_2\text{C}_4\text{H}$, $\text{Si}_2\text{C}_4\text{H}_2$, $\text{Si}_2\text{C}_6\text{H}$, and $\text{Si}_2\text{C}_6\text{H}_2$.

2B_2 , 8.97 eV, as compared to that for 2A_1 , 9.31 eV. This means that the 2A_1 cationic state has better Franck–Condon factors for ionization from the neutral silacyclopentenylidene SiC_2H_2 than the 2B_2 state and the comparison with the experimental PIE curve supports the hypothesis that the 2A_1 state of the ion was actually produced.

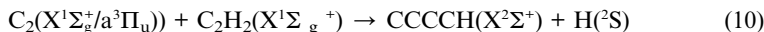
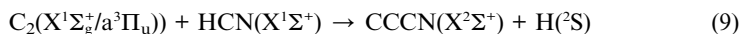
For SiC_2H , the story is not so straightforward. Calculations show the lowest lying isomer in the neutral channel is of the linear SiCCH radical form with $C_{\infty v}$ symmetry and ${}^2\Pi$ doublet state with VIE and AIE of 7.3 eV in both cases. Note that Ketvirtis *et al.*¹¹⁵ calculated an AIE of 7.06 eV for this isomer at the QCISD(T)-(full) level. From our PIE it would appear that signal arises from around 8.0 eV above the base line and starts rising around 9.0 eV. A C_s , ${}^2A'$ cyclic isomer is calculated to lie 29.3 kJ mol⁻¹ above the linear ground state. Calculations show that this state upon ionization rearranges to a linear SiCCH cation holding $C_{\infty v}$ symmetry with VIE and AIE of 8.10 eV and 6.96 eV, respectively. It is plausible that these states because of bad Franck–Condon factors do not show much intensity in the ionized cationic states. The isomers which have calculated ionization energies around 9.0 eV, include chain C_s -symmetric CCSiH and cyclic non-planar HSiCC , lying 192.5 and 175.8 kJ mol⁻¹ above the lowest SiCCH structure. Although these high-energy isomers seem unlikely to be populated in the molecular beam, a plausible assignment of the observed PIE can be made based on the chain CCSiH isomer with calculated VIE and AIE of 9.54 and 9.02 eV, respectively. It should be noted that CCSiH can be produced directly from the L shaped isomer of SiC_2H_2 by the C–H bond cleavage. As the low-lying L shaped SiC_2H_2 isomer has not been observed in the PIE spectra, it is possible that it does not survive and dissociates to CCSiH , which in turn gives rise to the PIE curve measured from SiC_2H . On the other hand, according to our calculations, the cyclic H– SiCC isomer with a VIE of 9.26 eV decomposes when ionized indicating bad Franck–Condon factors for ionization.

There are very few measurements in the literature to which we can compare our measured appearance energies for the SiC systems. Drowart *et al.*¹¹⁶ reported electron impact ionization results for SiC_2 , Si_2C , Si_2C_2 , and Si_3C to be 10.2, 9.2, 8.2, and 8.2 eV respectively with quoted errors of ± 0.3 eV. Our measurements for SiC_2 and Si_2C_2 fall outside these error bars. Schmude and Gingerich¹¹⁷ also reported electron impact appearance energies of SiC_2 (10.4 ± 0.3 eV), Si_2C (9.5 ± 0.5 eV), Si_2C_2 (8.8 ± 0.5 eV) and Si_3C (7.9 ± 0.5 eV). The value for SiC_2 falls outside the error limits compared to our measured value, and the relatively large errors in these electron impact measurements for the other species do not allow for reliable thermodynamic information to be extracted. Furthermore, the value for the silicon dimer (Si_2) measured in both electron impact measurements, 7.0 ± 0.5 eV and 7.4 ± 0.3 eV, fall well outside a recent VUV photoionization determination of 7.92 ± 0.05 eV reported by our group.¹¹⁸ A recent theoretical calculation¹¹⁹ at the DFT B3LYP/6-311G(3df) level report ionization energies of 9.69 eV (linear SiCC), 9.79 eV (triangular CSiC), 9.18 eV (linear SiCSi), 9.19 eV (triangular SiCSi), and 8.97 eV (rhombus Si_2C_2). These ionization energies agree well with our experimental results and, since the calculations are likely to be vertical in nature, would suggest good Franck–Condon factors for ionization. Their calculated value of 7.81 eV for rhomboidal Si_2C_2 does not agree with our measured value of 8.4 eV and could likely arise from a different geometry being present in our molecular beam. The agreement with the other values does suggest that our measured ionization energies are more reliable than the early electron impact measurements. In terms of structure, it is widely believed that SiC_2 exists in the cyclic form and our results would indicate that this is indeed possible. A recent LDA-DFT study by Pradhan and Ray¹²⁰ report adiabatic ionization energies of 10.38–10.78 eV (SiC_2), 9.629 eV (Si_2C), 8.26 eV (Si_2C_2), and 8.68 eV (Si_3C) which are systematically above our measured energies suggesting an error in the local density approximation adopted by these authors. Our measured ionization energy of 9.2 eV for Si_2C agrees extremely well with the calculated adiabatic value of 9.2 ± 0.2 eV at various levels of theory for a transition to a linear ${}^2\Sigma_u^+$ state in the cation.¹²¹ The same authors also calculated ionization energies for Si_3C using similar

methods and suggest a vertical IE of 8.2 ± 0.2 eV for a $C_{2v}^1A_1$ state rhomboid structure transition to a $C_{2v}^2B_2$ state in the cation. They also suggest that the geometry of the neutral varies considerably from the cation leading to poor Franck–Condon factors and an adiabatic ionization energy of 7.8 ± 0.2 eV. In this particular case our appearance energy of 8.4 eV does not fall in with this prediction, however, the shape of the PIE curve is not steep but a gentle rise suggesting poor Franck–Condon factors for this species. For Si_2C_2 , a charge transfer energy bracketing method¹²² posits the ionization energy of 8.24 ± 0.2 eV which does not agree with our value of 8.95 eV. For the unrelaxed ion in the charge bracketing measurement, an ionization energy of 9.35 ± 0.1 eV was measured. It is possible that there was incomplete relaxation of the ion in the time frame of the charge bracketing experiment giving rise to a lower ionization energy. Ignatyev and Schaefer¹²² report values of the ionization energies to the lowest energy state of the cation (${}^2\Pi_g$) holding linear structure and the next highest state (2A_g), a slightly distorted rhombic structure which is similar in structure to the neutral ground state. This rhombic transition could be what is observed in our photoionization experiment as it has been suggested by numerous theoretical calculations¹²³ that the linear Si–C–C–Si and a rhombic structure are almost degenerate in energy. It is also interesting to point out that Yadav *et al.*¹¹⁹ calculate an IE of 8.97 eV for this transition which is in very good agreement with our measured appearance energy. For Si_2C_3 , Si_2C_4 , Si_2C_5 , Si_2C_6 , Si_3C_2 , and Si_4C_2 , there are no experimental or theoretical data on ionization energies in the literature to the best of our knowledge, and the results reported here are the first experimental determinations. There could be multiple isomers present in the molecular beam, coupled with different Franck–Condon factors for these isomers and these are probably reflected in the gentle rise and absence of sharp onsets in this set of PIE curves.

5. Conclusions

At this *Faraday Discussion*, we presented three research fields of interest to explore the chemical evolution of Titan's atmosphere and surface. First, we explored the chemical dynamics of simple diatomic radicals (dicarbon, methyldiyne) utilizing the crossed molecular beams method. This versatile experimental technique can be applied to study reactions relevant to the atmospheres of planets and their moons as long as intense and stable supersonic beam sources of the reactant species exist. By focusing on reactions of dicarbon with hydrogen cyanide, we could untangle for the first time the contribution of dicarbon in its singlet ground and first excited triplet states. These results were applied to understand and re-analyze the data of crossed beam reactions of the isoelectronic dicarbon plus acetylene reaction. The reactions of dicarbon with hydrogen cyanide (HCN) and acetylene (C_2H_2) lead to doublet radical by hydrogen emission:



These radicals can react further with unsaturated hydrocarbons to form highly unsaturated hydrocarbons and nitriles, which could act as precursor molecules to the organic aerosol layers. Note that the kinetics of the 1,3-butadiynyl radical reactions with unsaturated hydrocarbons are very fast even at low temperatures relevant to Titan's atmosphere.¹²⁴ However, the reaction products are elusive. Crossed beam experiments are planned to untangle the dynamics of these reactions in a similar way as those of the important methyldiyne reactions.

Second, we investigated the interaction of ionizing radiation in form of energetic electrons with organic molecules ethane and propane sequestered on Titan's surface. These experiments presented compelling evidence that even at irradiation exposures equivalent to about 44 years on Titan's surface, aliphatic-like organic residues can be

produced. Scaling this to a geological time scale of, for instance, 10^9 years on Titan, this results in case of propane irradiation exposure into an accumulation of 1.5 meter organic polymer per cm^2 . Therefore, our laboratory experiments show that in principle, propane can be converted to aliphatic-type solid polymers over geological timescales on Titan's surface *via* interaction with cosmic ray particles. It is important in future models of Titan to account for the radiation-induced modification of Titan's surface and to evaluate objectively its contribution compared to deposition from organics by 'sedimentation' from higher atmospheric layers. Nevertheless, a galactic cosmic ray driven chemistry will certainly influence Titan's overall hydrocarbon budget.

Finally, we investigated how Titan's nascent chemical inventory can be altered by an *external* influx of matter as supplied by (micro)meteorites and possibly comets. For this, we simulated the ablation process in Titan's atmosphere, which can lead to ground and electronically excited atoms of, for instance, the principal constituents of silicates like iron, silicon, and magnesium, in laboratory experiments. By ablating silicon species and seeding the ablated species in acetylene carrier gas, which also acts as a reactant, we produced organo silicon species, which were then photoionized utilizing tunable VUV radiation from the Advanced Light Source. In combination with electronic structure calculations, the structures and ionization energies of distinct organo-silicon species were elucidated. We plan to expand these studies also to iron and magnesium-bearing species in the near future.

In summary, laboratory experiments such as crossed molecular beams scattering experiments, surface scattering studies, and laser ablation studies coupled with electronic structure calculations and VUV photoionization provide a powerful tool to shed light on Titan's chemistry not only of the atmosphere, but also of Titan's surface. To understand Titan's chemistry comprehensively, surfaces, aerosols, and the gas phase cannot be treated separately, but must be incorporated into a single model. Naturally, this will present a nice challenge to the modeling community. However, by providing feedback between experimentalists, modelers, and observers, in principle these models can be refined iteratively until a satisfactory agreement between experiments, observations, and models is reached – not only with respect to Titan, but for any body in our Solar System.

Acknowledgements

The crossed beam (P. M., C. E., F. Z., X. G., R. I. K.) and electronic structure calculations (S. P. K., A. M. M.) were supported by the Chemistry Division of the US National Science Foundation within the framework of the Collaborative Research in Chemistry (CRC) Program (NSF-CRC CHE-0627854). The experiments at the Advanced Light Source (OK, MA) was supported by the Director, Office of Energy Research, Office of Basic Energy Sciences, and Chemical Sciences Division of the U.S. Department of Energy under contracts No. DE-AC02-05CH11231.

References

- 1 D. Cordier, O. Mousis, J. I. Lunine, P. Lavvas and V. Vuitton, *Astrophys. J.*, 2009, **707**, L128.
- 2 A. Coustenis and M. Hirtzig, *Res. Astron. Astrophys.*, 2009, **9**, 249; J. L. Mitchell, *J. Geophys. Res.*, 2008, **113**, E08015.
- 3 L. Le Corre, S. Le Mouelic, C. Sotin, J. P. Combe, S. Rodriguez, J. W. Barnes, R. H. Brown, B. J. Buratti, R. Jaumann, J. Soderblom, L. A. Soderblom, R. Clark, K. H. Baines and P. D. Nicholson, *Planet. Space Sci.*, 2009, **57**, 870.
- 4 C. Elachi, S. Wall, M. Allison, Y. Anderson, R. Boehmer, P. Callahan, P. Encrenaz, E. Flamini, G. Franceschetti, Y. Gim, G. Hamilton, S. Hensley, M. Janssen, W. Johnson, K. Kelleher, R. Kirk, R. Lopes, R. Lorenz, J. Lunine, D. Muhleman, S. Ostro, F. Paganelli, G. Picardi, F. Posa, L. Roth, R. Seu, S. Shaffer, L. Soderblom,

- B. Stiles, E. Stofan, S. Vetrilla, R. West, C. Wood, L. Wye and H. Zebker, *Science*, 2005, **308**, 970.
- 5 E. L. Schaller, H. G. Roe, T. Schneider and M. E. Brown, *Nature*, 2009, **460**, 873.
- 6 C. A. Griffith, *Nature*, 2006, **442**, 362.
- 7 P. Lavvas, R. V. Yelle and V. Vuitton, *Icarus*, 2009, **201**, 626.
- 8 Y. Sekine, H. Imanaka, T. Matsui, B. N. Khare, E. L. O. Bakes, C. P. McKay and S. Sugita, *Icarus*, 2008, **194**, 186.
- 9 M. G. Trainer, A. A. Pavlov, H. L. DeWitt, J. L. Jimenez, C. P. McKay, O. B. Toon and M. A. Tolbert, *Proc. Natl. Acad. Sci. U. S. A.*, 2006, **103**, 18035.
- 10 T. B. McCord, G. B. Hansen, B. J. Buratti, R. N. Clark, D. P. Cruikshank, E. D'Aversa, C. A. Griffith, E. K. H. Baines, R. H. Brown, C. M. Dalle Ore, G. Filacchione, V. Formisano, C. A. Hibbitts, R. Jaumann, J. I. Lunine, R. M. Nelson and C. Sotin, *Planet. Space Sci.*, 2006, **54**, 1524.
- 11 A. Coustenis, B. Bezard and D. Gautier, *Icarus*, 1989, **80**, 54; A. Coustenis, B. Bezard, D. Gautier, A. Marten and R. Samuelson, *Icarus*, 1991, **89**, 152.
- 12 A. Coustenis, R. K. Achterberg, B. J. Conrath, D. E. Jennings, A. Marten, D. Gautier, C. A. Nixon, F. M. Flasar, N. A. Teanby, B. Bezard, R. E. Samuelson, R. C. Carlson, E. Lellouch, G. L. Bjoraker, P. N. Romani, F. W. Taylor, P. G. J. Irwin, T. Fouchet, A. Hubert, G. S. Orton, V. G. Kunde, S. Vinatier, J. Mondellini, M. M. Abbas and R. Courtin, *Icarus*, 2007, **189**, 35.
- 13 A. Canosa, A. Paramo, S. D. Le Picard and I. R. Sims, *Icarus*, 2007, **187**, 558.
- 14 X. Gu, Y. Guo, F. Zhang, A. M. Mebel and R. I. Kaiser, *Faraday Discuss.*, 2006, **133**, 245.
- 15 A. Canosa, I. R. Sims, D. Travers, I. W. M. Smith and B. R. Rowe, *Astron. Astrophys.*, 1997, **323**, 644.
- 16 R. I. Kaiser and N. Balucani, *Acc. Chem. Res.*, 2001, **34**, 699.
- 17 X. Gu, Y. S. Kim, R. I. Kaiser, A. M. Mebel, M. C. Liang and Y. L. Yung, *Proc. Natl. Acad. Sci. U. S. A.*, 2009, **106**, 16078.
- 18 F. Zhang, Y. S. Kim, R. I. Kaiser, S. P. Krishtal and A. M. Mebel, *J. Phys. Chem.*, 2009, **113**, 11167.
- 19 X. Zhang, J. M. Ajello and Y. L. Yung, *Astrophys. J.*, **708**, L18; E. H. Wilson and S. K. Atreya, *J. Phys. Chem.*, 2009, **113**, 11221; E. Hebrard, M. Dobrijevic, P. Pernot, N. Carrasco, A. Bergeat, K. M. Hickson, A. Canosa, S. D. Le Picard and I. R. Sims, *J. Phys. Chem.*, 2009, **113**, 11227; J. Cui, R. V. Yelle, V. Vuitton, J. H. Waite, Jr., W. T. Kasprzak, D. A. Gell, H. B. Niemann, I. C. F. Muller-Wodarg, N. Borggren, G. G. Fletcher, E. L. Patrick, E. Raaen and B. A. Magee, *Icarus*, 2009, **200**, 581; V. A. Krasnopolsky, *Icarus*, 2009, **201**, 226.
- 20 D. Cordier, O. Mousis, J. I. Lunine, A. Moudens and V. Vuitton, *Astrophys. J.*, 2008, **689**, L61; J. I. Lunine and S. K. Atreya, *Nat. Geosci.*, 2008, **1**, 159; H. Imanaka and M. A. Smith, *J. Phys. Chem.*, 2009, **113**, 11187; V. Vuitton, J. F. Doussin, Y. Benilan, F. Raulin and M. C. Gazeau, *Icarus*, 2006, **185**, 287.
- 21 C. A. Arrington, C. Ramos, A. D. Robinson and T. S. Zwier, *J. Phys. Chem.*, 1999, **103**, 1294.
- 22 D. W. Clarke and J. P. Ferris, *Icarus*, 1997, **127**, 158.
- 23 A. Aflalaye, R. Sternberg, F. Raulin and C. Vidal-Madjar, *J. Chromatogr., A*, 1995, **708**, 283; R. Sternberg, C. Szopa, D. Coscia, S. Zubrzycki, F. Raulin, C. Vidal-Madjar, H. Niemann and G. Israel, *J. Chromatogr., A*, 1999, **846**, 307; A. Aflalaye, R. Sternberg, D. Coscia, F. Faulin and C. Vidal-Madjar, *J. Chromatogr., A*, 1997, **761**, 195.
- 24 F. Zhang, S. Kim, R. I. Kaiser, A. Jamal and A. M. Mebel, *J. Chem. Phys.*, 2009, **130**, 234308.
- 25 D. Chastaing, P. L. James, I. R. Sims and I. W. M. Smith, *Faraday Discuss.*, 1998, **109**, 165; D. Carty, V. Le Page, I. R. Sims and I. W. M. Smith, *Chem. Phys. Lett.*, 2001, **344**, 310.
- 26 W. M. Jackson and A. Scodinu, *Astrophys. Space Sci. Libr.*, 2004, **311**, 85; G. Apaydin, W. H. Fink and W. M. Jackson, *J. Chem. Phys.*, 2004, **121**, 9368; N. S. Smith and F. Raulin, *J. Geophys. Res.*, 1999, **104**, 1873; N. S. Smith, Y. Benilan and P. Bruston, *Planet. Space Sci.*, 1998, **46**, 1215; R. J. Cody, P. N. Romani, F. L. Nesbitt, M. A. Iannone, D. C. Tardy and L. J. Stief, *J. Geophys. Res.*, 2003, **108**, 5119; R. J. Cody, W. A. Payne, Jr., R. P. Thorn, Jr., F. L. Nesbitt, M. A. Iannone, D. C. Tardy and L. J. Stief, *J. Phys. Chem.*, 2002, **106**, 6060; G. P. Smith, *Chem. Phys. Lett.*, 2003, **376**, 381; M. J. Davis and S. J. Klippenstein, *J. Phys. Chem.*, 2002, **106**, 5860; K. Seki and H. Okabe, *J. Phys. Chem.*, 1993, **97**, 5284; B. A. Balko, J. Zhang and Y. T. Lee, *J. Chem. Phys.*, 1991, **94**, 7958; A. Lauter, K. S. Lee, K. H. Jung, R. K. Vatsa, J. P. Mittal and H. R. Volpp, *Chem. Phys. Lett.*, 2002, **358**, 314; A. M. Wodtke and Y. T. Lee, *J. Phys. Chem.*, 1985, **89**, 4744; J. Segall, Y. Wen,

- R. Lavi, R. Singer and C. Wittig, *J. Phys. Chem.*, 1991, **95**, 8078; H. Okabe, *J. Chem. Phys.*, 1983, **78**, 1312; S.-H. Lee, Y. T. Lee and X. Yang, *J. Chem. Phys.*, 2004, **120**, 10983; E. F. Cromwell, A. Stolow, M. J. J. Vrakking and Y. T. Lee, *J. Chem. Phys.*, 1992, **97**, 4029; B. A. Balko, J. Zhang and Y. T. Lee, *J. Chem. Phys.*, 1992, **97**, 935; A. H. H. Chang, A. M. Mebel, X. M. Yang, S. H. Lin and Y. T. Lee, *Chem. Phys. Lett.*, 1998, **287**, 301; J. J. Lin, D. W. Hwang, Y. T. Lee and X. Yang, *J. Chem. Phys.*, 1998, **109**, 2979; A. Pena-Gallego, E. Martinez-Nunez and S. A. Vazquez, *Chem. Phys. Lett.*, 2002, **353**, 418.
- 27 J.-H. Wang, K. Liu, Z. Min, H. Su, R. Bersohn, J. Preses and J. Z. Larese, *J. Chem. Phys.*, 2000, **113**, 4146.
- 28 A. Paramo, A. Canosa, S. D. Le Picard and I. R. Sims, *J. Phys. Chem. A*, 2008, **112**, 9591.
- 29 X. Gu, R. I. Kaiser, A. M. Mebel, V. V. Kislov, S. J. Klippenstein, L. B. Harding, M. C. Liang and Y. L. Yung, *Astrophys. J.*, 2009, **701**, 1797.
- 30 N. Balucani, F. Leonori, R. Petrucci, K. M. Hickson and P. Casavecchia, *Phys. Scr.*, 2008, **78**, 058117.
- 31 X. Gu, Y. Guo, A. M. Mebel and R. I. Kaiser, *J. Phys. Chem.*, 2006, **110**, 11265.
- 32 J. R. McNesby and H. Okabe, *Adv. Photochem.*, 1964, 157.
- 33 A. H. Laufer and J. R. McNesby, *J. Chem. Phys.*, 1968, **49**, 2272.
- 34 R. Gorden, Jr. and P. Ausloos, *J. Chem. Phys.*, 1967, **46**, 4823.
- 35 R. E. Rebert and P. Ausloos, *J. Photochem.*, 1972, **1**, 171.
- 36 T. C. Slinger and G. Black, *J. Chem. Phys.*, 1982, **77**, 2432.
- 37 Y. L. Yung and W. B. DeMore, *Photochemistry of Planetary Atmosphere*, Oxford University Press, New York, 1997.
- 38 M. D. Lodriguito, G. Lendvay and G. C. Schatz, *J. Chem. Phys.*, 2009, **131**, 224320.
- 39 Y. Zhang, K. Yuan, S. Yu and X. Yang, *J. Phys. Chem. Lett.*, 2010, **1**, 475.
- 40 L. C. Lee and C. C. Chiang, *J. Chem. Phys.*, 1983, **78**, 688.
- 41 D. H. Mordant, I. R. Lambert, G. P. Morley, M. N. R. Ashfold, R. N. Dixon, C. M. Western, L. Schnieder and K. H. Welge, *J. Chem. Phys.*, 1993, **98**, 2054.
- 42 R. A. Brownsword, M. Hillenkamp, T. Laurent, R. K. Vatsa, H. R. Volpp and J. Wolfrum, *Chem. Phys. Lett.*, 1997, **266**, 259.
- 43 A. M. Mebel, S.-H. Lin and C.-H. Chang, *J. Chem. Phys.*, 1997, **106**, 2612.
- 44 A. J. R. Heck, R. N. Zare and D. W. Chandler, *J. Chem. Phys.*, 1996, **104**, 4019; A. J. R. Heck, R. N. Zare and D. W. Chandler, *J. Chem. Phys.*, 1996, **104**, 3399; J.-H. Wang and K. Liu, *J. Chem. Phys.*, 1998, **109**, 7105.
- 45 F. Goulay, A. J. Trevitt, G. Meloni, T. M. Selby, D. L. Osborn, C. A. Taatjes, L. Vereecken and S. R. Leone, *J. Am. Chem. Soc.*, 2009, **131**, 993.
- 46 O. F. Sigurbjornsson and R. Signorell, *Phys. Chem. Chem. Phys.*, 2008, **10**, 6211.
- 47 M. G. Tomasko, L. R. Doose, L. E. Dafoe and C. See, *Icarus*, 2009, **204**, 271.
- 48 C. Sagan and W. R. Thompson, *Icarus*, 1984, **59**, 133.
- 49 G. J. Molina-Cuberos, J. J. Lopez-Moreno, R. Rodrigo, L. M. Lara and K. O'Brien, *Planet. Space Sci.*, 1999, **47**, 1347.
- 50 M.-C. Liang, Y. L. Yung and D. E. Shemansky, *Astrophys. J.*, 2007, **661**, L199.
- 51 S. H. Abbas and D. Schulze-Makuch, Abstracts of Papers, 234th ACS National Meeting, Boston, MA, United States, August 19–23, 2007, 2007, GEOC; J. Parnell, M. Baron and P. Lindgren, *J. Geochem. Explor.*, 2006, **89**, 322; N. Artemieva and J. Lunine, *Icarus*, 2003, **164**, 471; R. D. Lorenz, *Meteorit. Planet. Sci.*, 2004, **39**, 617; N. Artemieva and J. I. Lunine, *Icarus*, 2005, **175**, 522; M. E. Kress and C. P. McKay, *Icarus*, 2004, **168**, 475.
- 52 S. M. Horst, V. Vuitton and R. V. Yelle, *J. Geophys. Res.*, 2008, **113**, E10006.
- 53 S. Petrie, *Icarus*, 2004, **171**, 199; W. D. Pesnell and J. M. Grebowsky, *Adv. Space Res.*, 2001, **27**, 1807.
- 54 S. Petrie and R. C. Dunbar, *AIP Conf. Proc.*, 2006, **855**, 272.
- 55 R. I. Kaiser and X. Gu, *J. Chem. Phys.*, 2009, **131**, 104311.
- 56 P. J. Linstrom and W. G. Mallard, in *NIST Standard Reference Database Number 69*, National Institute of Standards and Technology, Gaithersburg, MD, June 2005.
- 57 K. Liu, *J. Chem. Phys.*, 2006, **125**, 132307; Y. T. Lee, *Atomic and Molecular Beam Methods*, Oxford University Press, Oxford, 1988; I. Kaiser Ralf, *Chem. Rev.*, 2002, **102**, 1309.
- 58 P. Casavecchia, G. Capozza and E. Segoloni, *Adv. Ser. Phys. Chem.*, 2004, **14**, 329.
- 59 M.-J. Nam, S.-E. Youn and J.-H. Choi, *J. Chem. Phys.*, 2006, **124**, 104307.
- 60 M. F. Witinski, M. Ortiz-Suarez and H. F. Davis, *J. Chem. Phys.*, 2006, **124**, 094307.
- 61 P. L. Houston, *J. Phys. Chem.*, 1996, **100**, 12757; M. Ahmed, D. S. Peterka and A. G. Suits, *Chem. Phys. Lett.*, 1999, **301**, 372; D. Townsend, W. Li, K. Lee Suk, L. Gross Richard and G. Suits Arthur, *J. Phys. Chem. A*, 2005, **109**, 8661; W. Li, C. Huang, M. Patel, D. Wilson and A. Suits, *J. Chem. Phys.*, 2006, **124**, 011102.
- 62 X. Liu, R. L. Gross and A. G. Suits, *J. Chem. Phys.*, 2002, **116**, 5341.

- 63 F. Goulay, D. L. Osborn, C. A. Taatjes, P. Zou, G. Meloni and S. R. Leone, *Phys. Chem. Chem. Phys.*, 2007, **9**, 4291; G. Meloni, T. M. Selby, F. Goulay, S. R. Leone, D. L. Osborn and C. A. Taatjes, *J. Am. Chem. Soc.*, 2007, **129**, 14019; D. L. Osborn, *Adv. Chem. Phys.*, 2008, **138**, 213; T. M. Selby, G. Meloni, F. Goulay, S. R. Leone, A. Fahr, C. A. Taatjes and D. L. Osborn, *J. Phys. Chem.*, 2008, **112**, 9366; C. A. Taatjes, N. Hansen, D. L. Osborn, K. Kohse-Hoeinghaus, T. A. Cool and P. R. Westmoreland, *Phys. Chem. Chem. Phys.*, 2008, **10**, 20; C. A. Taatjes, D. L. Osborn, T. A. Cool and K. Nakajima, *Chem. Phys. Lett.*, 2004, **394**, 19.
- 64 M. Alagia, N. Balucani, L. Cartechini, P. Casavecchia, E. H. van Kleef, G. G. Volpi, F. J. Aoiz, L. Banares and D. W. Schwenke, *et al.*, *Science*, 1996, **273**, 1519; D. Skouteris, H.-J. Werner, F. J. Aoiz, L. Banares, J. F. Castillo, M. Menendez, N. Balucani, L. Cartechini and P. Casavecchia, *J. Chem. Phys.*, 2001, **114**, 10662; N. Balucani, D. Skouteris, G. Capozza, E. Segoloni, P. Casavecchia, M. H. Alexander, G. Capecci and H.-J. Werner, *Phys. Chem. Chem. Phys.*, 2004, **6**, 5007.
- 65 S.-H. Lee, F. Dong and K. Liu, *J. Chem. Phys.*, 2006, **125**, 133106.
- 66 B. D. Bean, J. D. Ayers, F. Fernandez-Alonso and R. N. Zare, *J. Chem. Phys.*, 2002, **116**, 6634.
- 67 N. Balucani, G. Capozza, E. Segoloni, A. Russo, R. Bobbenkamp, P. Casavecchia, T. Gonzalez-Lezana, E. J. Rackham, L. Banares and F. J. Aoiz, *J. Chem. Phys.*, 2005, **122**, 234309.
- 68 L. A. Pederson, G. C. Schatz, T.-S. Ho, T. Hollebeek, H. Rabitz, L. B. Harding and G. Lendvay, *J. Chem. Phys.*, 1999, **110**, 9091; N. Balucani, M. Alagia, L. Cartechini, P. Casavecchia, G. G. Volpi, L. A. Pederson and G. C. Schatz, *J. Phys. Chem.*, 2001, **105**, 2414; N. Balucani, L. Cartechini, G. Capozza, E. Segoloni, P. Casavecchia, G. G. Volpi, F. Javier Aoiz, L. Banares, P. Honvault and J.-M. Launay, *Phys. Rev. Lett.*, 2002, **89**, 013201; N. Balucani, P. Casavecchia, L. Banares, F. J. Aoiz, T. Gonzalez-Lezana, P. Honvault and J.-M. Launay, *J. Phys. Chem.*, 2006, **110**, 817.
- 69 N. Balucani, P. Casavecchia, F. J. Aoiz, L. Banares, J. F. Castillo and V. J. Herrero, *Mol. Phys.*, 2005, **103**, 1703; D. J. Garton, A. L. Brunsvold, T. K. Minton, D. Troya, B. Maiti and G. C. Schatz, *J. Phys. Chem.*, 2006, **110**, 1327; M. Alagia, N. Balucani, L. Cartechini, P. Casavecchia, E. H. van Kleef, G. G. Volpi, P. J. Kuntz and J. J. Sloan, *J. Chem. Phys.*, 1998, **108**, 6698; S. K. Gray, E. M. Goldfield, G. C. Schatz and G. G. Balint-Kurti, *Phys. Chem. Chem. Phys.*, 1999, **1**, 1141; F. J. Aoiz, L. Banares, J. F. Castillo, V. J. Herrero, B. Martinez-Haya, P. Honvault, J. M. Launay, X. Liu, J. J. Lin, S. A. Harich, C. C. Wang and X. Yang, *J. Chem. Phys.*, 2002, **116**, 10692.
- 70 S. H. Lee and K. Liu, *Appl. Phys. B: Lasers Opt.*, 2000, **71**, 627.
- 71 M. Alagia, N. Balucani, P. Casavecchia, D. Stranges and G. G. Volpi, *J. Chem. Phys.*, 1993, **98**, 8341.
- 72 B. R. Strazisar, C. Lin and H. F. Davis, *Science*, 2000, **290**, 958.
- 73 T. Takayanagi and G. C. Schatz, *J. Chem. Phys.*, 1997, **106**, 6227.
- 74 J. M. Bowman and G. C. Schatz, *Annu. Rev. Phys. Chem.*, 1995, **46**, 169.
- 75 B. Zhang, W. Shiu, J. J. Lin and K. Liu, *J. Chem. Phys.*, 2005, **122**, 131102; X. Liu and A. G. Suits, *Adv. Ser. Phys. Chem.*, 2004, 105; Q. Ran, C. H. Yang, Y. T. Lee, I. C. Lu, G. Shen, L. Wang and X. Yang, *J. Chem. Phys.*, 2005, **122**, 044307; G. Capozza, E. Segoloni, F. Leonori, G. G. Volpi and P. Casavecchia, *J. Chem. Phys.*, 2004, **120**, 4557; D. Troya, G. C. Schatz, D. J. Garton, A. L. Brunsvold and T. K. Minton, *J. Chem. Phys.*, 2004, **120**, 731; A. M. Mebel, R. I. Kaiser and Y. T. Lee, *J. Am. Chem. Soc.*, 2000, **122**, 1776; R. I. Kaiser, N. Balucani, O. Asvany and Y. T. Lee, *Symp. – Int. Astron. Union*, 2000, **197**, 251; N. Balucani, A. M. Mebel, Y. T. Lee and R. I. Kaiser, *J. Phys. Chem. A*, 2001, **105**, 9813; R. I. Kaiser, T. N. Le, T. L. Nguyen, A. M. Mebel, N. Balucani, Y. T. Lee, F. Stahl, P. v. R. Schleyer and H. F. Schaefer, III, *Faraday Discuss.*, 2001, **119**, 51; R. I. Kaiser, O. Asvany and Y. T. Lee, *Planet. Space Sci.*, 2000, **48**, 483; R. I. Kaiser, O. Asvany, Y. T. Lee, H. F. Bettinger, P. v. R. Schleyer and H. F. Schaefer, III, *J. Chem. Phys.*, 2000, **112**, 4994; L. Vereecken, J. Peeters, F. Bettinger Holger, I. Kaiser Ralf, R. v. Schleyer Paul and F. Schaefer Henry, 3rd, *J. Am. Chem. Soc.*, 2002, **124**, 2781; J. Zhou, B. Zhang, J. J. Lin and K. Liu, *Mol. Phys.*, 2005, **103**, 1757; W. Shiu, J. J. Lin, K. Liu, M. Wu and D. H. Parker, *J. Chem. Phys.*, 2004, **120**, 117; J. Zhou, W. Shiu, J. J. Lin and K. Liu, *J. Chem. Phys.*, 2004, **120**, 5863; W. Shiu, J. J. Lin and K. Liu, *Phys. Rev. Lett.*, 2004, **92**, 103201; R. I. Kaiser, A. M. Mebel, A. H. H. Chang, S. H. Lin and Y. T. Lee, *J. Chem. Phys.*, 1999, **110**, 10330; N. Balucani, H. Y. Lee, A. M. Mebel, Y. T. Lee and R. I. Kaiser, *J. Chem. Phys.*, 2001, **115**, 5107; H. F. Davis, J. Shu, S. Peterka Darcy and M. Ahmed, *J. Chem. Phys.*, 2004, **121**, 6254; R. L. Gross, X. Liu and A. G. Suits, *Chem. Phys. Lett.*, 2003, **376**, 710; X. Liu, R. L. Gross, G. E. Hall, J. T. Muckerman and A. G. Suits, *J. Chem. Phys.*, 2002, **117**, 7947; J. Shu, J. J. Lin, Y. T. Lee and X. Yang, *J. Chem. Phys.*, 2001, **115**, 849;

- P. Casavecchia, G. Capozza, E. Segoloni, F. Leonori, N. Balucani and G. G. Volpi, *J. Phys. Chem.*, 2005, **109**, 3527; C. C. Wang, J. Shu, J. J. Lin, Y. T. Lee, X. Yang, T. L. Nguyen and A. M. Mebel, *J. Chem. Phys.*, 2002, **116**, 8292; Y.-C. Sun, I. T. Wang, T. L. Nguyen, H.-F. Lu, X. Yang and A. M. Mebel, *J. Phys. Chem.*, 2003, **107**, 6986; R. I. Kaiser, Y. T. Lee and A. G. Suits, *J. Chem. Phys.*, 1995, **103**, 10395; R. I. Kaiser, D. Stranges, Y. T. Lee and A. G. Suits, *J. Chem. Phys.*, 1996, **105**, 8721; R. I. Kaiser, C. Ochsenfeld, M. Head-Gordon, Y. T. Lee and A. G. Suits, *J. Chem. Phys.*, 1997, **106**, 1729; R. I. Kaiser, D. Stranges, Y. T. Lee and A. G. Suits, *Astrophys. J.*, 1997, **477**, 982; C. Ochsenfeld, R. I. Kaiser, Y. T. Lee, A. G. Suits and M. Head-Gordon, *J. Chem. Phys.*, 1997, **106**, 4141; R. I. Kaiser, C. Ochsenfeld, M. Head-Gordon and Y. T. Lee, *Astrophys. J.*, 1999, **510**, 784.
- 76 R. Z. Hinrichs, P. A. Willis, H. U. Stauffer, J. J. Schroden and H. F. Davis, *J. Chem. Phys.*, 2000, **112**, 4634; H. U. Stauffer, R. Z. Hinrichs, J. J. Schroden and H. F. Davis, *J. Phys. Chem.*, 2000, **104**, 1107; J. J. Schroden, C. C. Wang and H. F. Davis, *J. Phys. Chem.*, 2003, **107**, 9295; R. Z. Hinrichs, J. J. Schroden and H. F. Davis, *J. Am. Chem. Soc.*, 2003, **125**, 860; J. J. Schroden, M. Teo and H. F. Davis, *J. Chem. Phys.*, 2002, **117**, 9258; R. Z. Hinrichs, J. J. Schroden and H. F. Davis, *J. Phys. Chem.*, 2008, **112**, 3010; J. J. Schroden and H. F. Davis, *Adv. Ser. Phys. Chem.*, 2004, **14**, 215; H. U. Stauffer, R. Z. Hinrichs, J. J. Schroden and H. F. Davis, *J. Chem. Phys.*, 1999, **111**, 10758.
- 77 M. J. Perri, A. L. Van Wyngarden, J. J. Lin, Y. T. Lee and K. A. Boering, *J. Phys. Chem.*, 2004, **108**, 7995; A. L. Van Wyngarden, K. A. Mar, K. A. Boering, J. J. Lin, Y. T. Lee, S.-Y. Lin, H. Guo and G. Lendvay, *J. Am. Chem. Soc.*, 2007, **129**, 2866; Y.-J. Lu, T. Xie, J.-W. Fang, H.-C. Shao and J. J. Lin, *J. Chem. Phys.*, 2008, **128**, 184302.
- 78 R. I. Kaiser, W. Sun and A. G. Suits, *J. Chem. Phys.*, 1997, **106**, 5288; R. I. Kaiser, C. Ochsenfeld, M. Head-Gordon and Y. T. Lee, *Science*, 1998, **279**, 1181; R. I. Kaiser, C. Ochsenfeld, M. Head-Gordon and Y. T. Lee, *J. Chem. Phys.*, 1999, **110**, 2391; R. I. Kaiser, I. Hahndorf, L. C. L. Huang, Y. T. Lee, H. F. Bettinger, P. v. R. Schleyer, H. F. Schaefer, III and P. R. Schreiner, *J. Chem. Phys.*, 1999, **110**, 6091; H. F. Bettinger, P. v. R. Schleyer, H. F. Schaefer, III, P. R. Schreiner, R. I. Kaiser and Y. T. Lee, *J. Chem. Phys.*, 2000, **113**, 4250; I. Hahndorf, Y. T. Lee, R. I. Kaiser, L. Vereecken, J. Peeters, H. F. Bettinger, P. R. Schreiner, P. v. R. Schleyer, W. D. Allen and H. F. Schaefer, III, *J. Chem. Phys.*, 2002, **116**, 3248; R. I. Kaiser, Y. T. Lee and A. G. Suits, *J. Chem. Phys.*, 1996, **105**, 8705; R. I. Kaiser, D. Stranges, H. M. Bevssek, Y. T. Lee and A. G. Suits, *J. Chem. Phys.*, 1997, **106**, 4945; I. Hahndorf, H. Y. Lee, A. M. Mebel, S. H. Lin, Y. T. Lee and R. I. Kaiser, *J. Chem. Phys.*, 2000, **113**, 9622; L. C. L. Huang, H. Y. Lee, A. M. Mebel, S. H. Lin, Y. T. Lee and R. I. Kaiser, *J. Chem. Phys.*, 2000, **113**, 9637; T. N. Le, H.-y. Lee, A. M. Mebel and R. I. Kaiser, *J. Phys. Chem. A*, 2001, **105**, 1847; T. L. Nguyen, A. M. Mebel and R. I. Kaiser, *J. Phys. Chem. A*, 2001, **105**, 3284; R. I. Kaiser, T. L. Nguyen, T. N. Le and A. M. Mebel, *Astrophys. J.*, 2001, **561**, 858; W. D. Geppert, C. Naulin, M. Costes, G. Capozza, L. Cartechini, P. Casavecchia and G. Gualberto Volpi, *J. Chem. Phys.*, 2003, **119**, 10607.
- 79 N. Balucani, O. Asvany, Y. T. Lee, R. I. Kaiser, N. Galland and Y. Hannachi, *J. Am. Chem. Soc.*, 2000, **122**, 11234; N. Balucani, O. Asvany, Y. T. Lee, R. I. Kaiser, N. Galland, M. T. Rayez and Y. Hannachi, *J. Comput. Chem.*, 2001, **22**, 1359; W. D. Geppert, F. Goulay, C. Naulin, M. Costes, A. Canosa, S. D. Le Picard and B. R. Rowe, *Phys. Chem. Chem. Phys.*, 2004, **6**, 566.
- 80 N. Balucani, L. Cartechini, M. Alagia, P. Casavecchia and G. G. Volpi, *J. Phys. Chem.*, 2000, **104**, 5655; N. Balucani, O. Asvany, A. H. H. Chang, S. H. Lin, Y. T. Lee, R. I. Kaiser, H. F. Bettinger, P. v. R. Schleyer and H. F. Schaefer, III, *J. Chem. Phys.*, 1999, **111**, 7457; R. I. Kaiser, C. C. Chiong, O. Asvany, Y. T. Lee, F. Stahl, P. v. R. Schleyer and H. F. Schaefer, III, *J. Chem. Phys.*, 2001, **114**, 3488; F. Stahl, P. v. R. Schleyer, H. F. Bettinger, R. I. Kaiser, Y. T. Lee and H. F. Schaefer, III, *J. Chem. Phys.*, 2001, **114**, 3476; R. I. Kaiser, F. Stahl, P. v. R. Schleyer and H. F. Schaefer, III, *Phys. Chem. Chem. Phys.*, 2002, **4**, 2950; F. Stahl, P. v. R. Schleyer, H. F. Schaefer, III and R. I. Kaiser, *Planet. Space Sci.*, 2002, **50**, 685; L. C. L. Huang, Y. T. Lee and R. I. Kaiser, *J. Chem. Phys.*, 1999, **110**, 7119; L. C. L. Huang, N. Balucani, Y. T. Lee, R. I. Kaiser and Y. Osamura, *J. Chem. Phys.*, 1999, **111**, 2857; N. Balucani, O. Asvany, A. H. H. Chang, S. H. Lin, Y. T. Lee, R. I. Kaiser, H. F. Bettinger, P. v. R. Schleyer and H. F. Schaefer, III, *J. Chem. Phys.*, 1999, **111**, 7472; N. Balucani, O. Asvany, Y. Osamura, L. C. L. Huang, Y. T. Lee and R. I. Kaiser, *Planet. Space Sci.*, 2000, **48**, 447; N. Balucani, O. Asvany, A. H. H. Chang, S. H. Lin, Y. T. Lee, R. I. Kaiser and Y. Osamura, *J. Chem. Phys.*, 2000, **113**, 8643; N. Balucani, O. Asvany, L. C. L. Huang, Y. T. Lee, R. I. Kaiser, Y. Osamura and H. F. Bettinger, *Astrophys. J.*, 2000, **545**, 892; L. C. L. Huang,

- O. Asvany, A. H. H. Chang, N. Balucani, S. H. Lin, Y. T. Lee, R. I. Kaiser and Y. Osamura, *J. Chem. Phys.*, 2000, **113**, 8656; R. I. Kaiser, *Eur. Space Agency, [Spec. Publ.]*, 2001, **SP-496**, 145; N. Balucani, O. Asvany, R. I. Kaiser and Y. Osamura, *J. Phys. Chem. A*, 2002, **106**, 4301.
- 81 R. I. Kaiser, J. W. Ting, L. C. L. Huang, N. Balucani, O. Asvany, Y. T. Lee, H. Chan, D. Stranges and D. Gee, *Rev. Sci. Instrum.*, 1999, **70**, 4185.
- 82 X. Gu and R. I. Kaiser, *Acc. Chem. Res.*, 2009, **42**, 290.
- 83 R. I. Kaiser and A. G. Suits, *Rev. Sci. Instrum.*, 1995, **66**, 5405.
- 84 F. Zhang, S. Kim and R. I. Kaiser, *Phys. Chem. Chem. Phys.*, 2009, **11**, 4707; R. I. Kaiser, C. Ochsenfeld, D. Stranges, M. Head-Gordon and Y. T. Lee, *Faraday Discuss.*, 1998, **109**, 183.
- 85 Y. Guo, A. M. Mebel, F. Zhang, X. Gu and R. I. Kaiser, *J. Phys. Chem. A*, 2007, **111**, 4914; F. Zhang, X. Gu, Y. Guo and R. I. Kaiser, *J. Org. Chem.*, 2007, **72**, 7597.
- 86 K. A. Berrington, K. L. Bell and Editors, Proceedings of the Second International Conference on Atomic and Molecular Data and Their Applications (ICAMDATA), held 26–30 March 2000, in Oxford England. [In: AIP Conf. Proc., 2000; 543] It is crucial to note that the ionization cross section drops almost linearly from its maximum toward lower electron energies (Wigner relation).
- 87 M. S. Weiss, University Of California, Berkeley, Berkeley, CA, 1986.
- 88 X. Gu, Y. Guo, E. Kawamura and R. I. Kaiser, *J. Vac. Sci. Technol., A*, 2006, **24**, 505.
- 89 A. M. Mebel and R. I. Kaiser, *Astrophys. J.*, 2002, **564**, 787.
- 90 F. Zhang, B. Jones, P. Maksyutenko, R. I. Kaiser, C. Chin, V. V. Kislov and A. M. Mebel, *J. Am. Chem. Soc.*, 2010, **132**, 2672.
- 91 M. Yamada, Y. Osamura and R. I. Kaiser, *Astron. Astrophys.*, 2002, **395**, 1031.
- 92 X. Tan, *CyberWit*, version 1.4, Santa Clara, 2004.
- 93 C. V. V. Prasad and P. F. Bernath, *Astrophys. J.*, 1994, **426**, 812; A. Tanabashi, T. Hirao, T. Amano and P. F. Bernath, *Astrophys. J. Suppl.*, 2007, **169**, 472.
- 94 M. Danielsson, P. Erman, A. Hishikawa, M. Larsson and E. Rachlew-Kaellne, *J. Chem. Phys.*, 1993, **98**, 9405.
- 95 P. Zou, J. Shu, T. J. Sears, G. E. Hall and S. W. North, *J. Phys. Chem. A*, 2004, **108**, 1482; W. S. McGivern, O. Sorkhabi, A. G. Suits, A. Derecskei-Kovacs and S. W. North, *J. Phys. Chem. A*, 2000, **104**, 10085.
- 96 R. Atkinson, D. L. Baulch, R. A. Cox, R. F. Hampson, Jr., J. A. Kerr and J. Troe, *J. Phys. Chem. Ref. Data*, 1992, **21**, 1125.
- 97 A. M. Mebel, Florida International University, unpublished results, 2009.
- 98 J. Luque, LIFBASE, see <http://www.sri.com/psd/lifbase/>.
- 99 C. J. Bennett, C. Jamieson, A. M. Mebel and R. I. Kaiser, *Phys. Chem. Chem. Phys.*, 2004, **6**, 735.
- 100 R. B. Bohn, S. A. Sandford, L. J. Allamandola and D. P. Cruikshank, *Icarus*, 1994, **111**, 151.
- 101 J. W. Stewart and R. I. La Rock, *J. Chem. Phys.*, 1958, **28**, 425.
- 102 D. Drouin, A. R. Couture, R. Gauvin, P. Hovington, P. Horny and H. Demers, *Monte Carlo Simulation of Electron Trajectory in Solids (CASINO ver 2.42)*, University of Sherbrook, Sherbrook, 2001.
- 103 P. A. Heimann, M. Koike, C. W. Hsu, D. Blank, X. M. Yang, A. G. Suits, Y. T. Lee, M. Evans and C. Y. Ng, *et al.*, *Rev. Sci. Instrum.*, 1997, **68**, 1945.
- 104 C. Nicolas, J. N. Shu, D. S. Peterka, M. Hochlaf, L. Poisson, S. R. Leone and M. Ahmed, *J. Am. Chem. Soc.*, 2006, **128**, 220–226.
- 105 R. I. Kaiser, L. Belau, S. R. Leone, M. Ahmed, Y. Wang, B. J. Braams and J. M. Bowman, *Chem. Phys. Chem.*, 2007, **8**, 1236.
- 106 A. D. Becke, *J. Chem. Phys.*, 1993, **98**, 5648; C. Lee, W. Yang and R. G. Parr, *Phys. Rev. B: Condens. Matter*, 1988, **37**, 785.
- 107 M. J. Frisch, G. W. Trucks, H. B. Schlegel, G. E. Scuseria, M. A. Robb, J. R. Cheeseman, V. G. Zakrzewski, J. A. Montgomery, Jr., R. E. Stratmann, J. C. Burant, S. Dapprich, J. M. Millam, A. D. Daniels, K. N. Kudin, M. C. Strain, O. Farkas, J. Tomasi, V. Barone, M. Cossi, R. Cammi, B. Mennucci, C. Pomelli, C. Adamo, S. Clifford, J. Ochterski, G. A. Petersson, P. Y. Ayala, Q. Cui, K. Morokuma, P. Salvador, J. J. Dannenberg, D. K. Malick, A. D. Rabuck, K. Raghavachari, J. B. Foresman, J. Cioslowski, J. V. Ortiz, A. G. Baboul, B. B. Stefanov, G. Liu, A. Liashenko, P. Piskorz, I. Komaromi, R. Gomperts, R. L. Martin, D. J. Fox, T. Keith, M. A. Al-Laham, C. Y. Peng, A. Nanayakkara, M. Challacombe, P. M. W. Gill, B. G. Johnson, W. Chen, M. W. Wong, J. L. Andres, C. Gonzalez, M. Head-Gordon, E. S. Replogle and J. A. Pople, *GAUSSIAN 98 (Revision A.11)*, Gaussian, Inc., Pittsburgh, PA, 2001.
- 108 R. D. Amos, A. Bernhardtsson, A. Berning, P. Celani, D. L. Cooper, M. J. O. Deegan, A. J. Dobbyn, F. Eckert, C. Hampel, G. Hetzer, P. J. Knowles, T. Korona, R. Lindh,

- A. W. Lloyd, S. J. McNicholas, F. R. Manby, W. Meyer, M. E. Mura, A. Nicklass, P. Palmieri, R. Pitzer, G. Rauhut, M. Schütz, U. Schumann, H. Stoll, A. J. Stone, R. Tarroni, T. Thorsteinsson and H.-J. Werner, *MOLPRO, a package of ab initio programs designed by H.-J. Werner and P. J. Knowles, Version 2002.6*, 2002.
- 109 R. I. Kaiser, in *Carbon-Centered Radicals: Structure, Dynamics and Reactivity*, ed. M. D. E. Fobes, Wiley, 2010, pp. 221.
- 110 S. B. Tejada and D. F. Eggers, Jr., *Spectrochim. Acta, Part A*, 1976, **32**, 1557.
- 111 R. L. Hudson, M. H. Moore and L. L. Raines, *Icarus*, 2009, **203**, 677.
- 112 Y. S. Kim, C. J. Bennett, L.-H. Chen, K. O'Brien and R. I. Kaiser, *Astrophys. J.*, 2010, **711**, 744.
- 113 M. A. Goodman, R. L. Sweany and R. L. Flurry, Jr., *J. Phys. Chem.*, 1983, **87**, 1753.
- 114 S. Ikuta, T. Saitoh and S. Wakamatsu, *J. Chem. Phys.*, 2004, **121**, 3478.
- 115 A. E. Ketvirtis, D. K. Bohme and A. C. Hopkinson, *J. Phys. Chem.*, 1995, **99**, 16121.
- 116 J. Drowart, G. de Maria and M. G. Inghram, *J. Chem. Phys.*, 1958, **29**, 1015.
- 117 R. W. Schmude, Jr. and K. A. Gingerich, *J. Phys. Chem.*, 1997, **101**, 2610.
- 118 O. Kostko, S. R. Leone, M. A. Duncan and M. Ahmed, *J. Phys. Chem. A*, 2010, **114**, 3176.
- 119 P. S. Yadav, R. K. Yadav, S. Agrawal and B. K. Agrawal, *J. Phys.: Condens. Matter*, 2006, **18**, 7085.
- 120 P. Pradhan and A. K. Ray, *Eur. Phys. J. D*, 2006, **37**, 393.
- 121 A. I. Boldyrev, J. Simons, V. G. Zakrzewski and W. von Niessen, *J. Phys. Chem.*, 1994, **98**, 1427.
- 122 D. C. Parent, *Int. J. Mass Spectrom. Ion Processes*, 1994, **138**, 307.
- 123 J. Hou and B. Song, *J. Chem. Phys.*, 2008, **128**, 154304.
- 124 C. Berteloite, S. D. Le Picard, P. Birza, M.-C. Gazeau, A. Canosa, Y. Benilan and I. R. Sims, *Icarus*, 2008, **194**, 746.